Johannes Opedal Kverno

Flexible operation of Francis turbines

Johannes Opedal Kverno

Doctoral thesis

NTNU
Norwegian University of
Science and Technology

NTNU
Norwegian University of
Science and Technology

Johannes Opedal Kverno

Flexible operation of Francis turbines

Thesis for the degree of Philosophiae Doctor

Trondheim, November 2023

Norwegian University of Science and Technology
Faculty of Engineering
Department of Energy and Process Engineering

NTNU
Norwegian University of
Science and Technology

Til minne om mormor,

Bjørg Opedal (1930-2022),

som ga meg det første ordentlige dyttet mot mine studier.

Preface

This thesis is the result of the authors work as a PhD candidate at the Waterpower Laboratory in the Department of Energy and Process Engineering (EPT) at the Norwegian University of Science and Technology (NTNU) in Trondheim, Norway. The presented work is a collection of papers written in the period of August 2019 to August 2023. The experimental work presented in this thesis was also conducted at the Waterpower Laboratory in collaboration with several master students throughout the course of the project. Due to the global pandemic putting a stop to planned conference attendances the ensuing publications and initial experimental plans were delayed. The research was conducted under the HydroFlex project which received funding from the European Union's Horizon 2020 research and innovation programme under grant agreement No 764011. As a part of HydroFlex, the research on the mechanical and hydraulic aspects of turbines were conducted in work package 3 with the partners the Norwegian University of Science and Technology (NTNU), EDR Medeso, Rainpower, Ss. Cyril and Methodius University in Skopje, and Luleå University of Technology. Professor Ole Gunnar Dahlhaug from NTNU has been the main supervisor for this work and research.

Abstract

With the planned cuts in emissions, more of the electric energy will have to come from renewable sources. Two of the largest potential sources are wind- and solar, which have the downside of also being intermittent and non-dispatchable. Since the electricity production must match the consumption, other energy producers in a grid must increase their rate of flexibility to compensate, of which hydropower is well suited to do. However, with more frequent start-stop cycles and high ramping, an increase in fatigue and failures of reaction turbines, such as Francis turbines, are to be expected, so being able to predict how much additional damage this new scheme of operation will cause is of high interest.

The primary objective for the thesis is to improve the understanding of how various operation schemes affects the Francis turbines through model experiments and onboard measurements of strain where runner blades are most prone to develop cracks.

Focused on presenting both an experimental setup and findings, this study delves into a comprehensive measurement campaign focused on a low specific speed Francis turbine. These experiments make up a critical part of the HydroFlex project, which seeks to validate simulations and gain deeper insights into the reduced lifespan of Francis turbines attributed to increase in fatigue loading resulting from flexible operation.

A setup and procedure for the calibration of runner blade mounted strain gauges has been developed, and the results is presented along with proposals for further improvements. This calibration setup consists of both a custom made jig to accurately load the runner blade in a predictable manner, and a nummerical counterpart in ANSYS Mechanical to simulate the stress and strain at the location of the strain gauges during the same loads.

Onboard measurement of the blade strain during operation in the model Francis turbine test rig at the Waterpower Laboratory (NTNU) is also presented with both some of the challenges encountered and also the final results obtained. The measurements span a wide range of speed- (n_{ED}) and discharge factors (Q_{ED}), and demonstrate the impact of these factors on the resulting dynamic strain.

Key challenges have been low sensitivity in the strain gauges first used and a high amount of electrical noise in the measurement chain. High susceptibility to small changes in the water temperature has also been a big challenge, causing the measured mean strain at no load to drift far away from its calibrated offset. Improvements to the strain gauge setup, and suggestions for how to capture mean trends despite temperature drift is discussed.

The results shows that while the peak to peak strain increases as the load is increased above the design point, the highest peak to peak occurs at part load. It is also seen how the trailing edge is impacted differently near the hub versus the shroud at off-design operating conditions due to which effects are the main source of the vibrations. The credibility of the results were also strengthened by an FFT analysis of the measured strain, as all the expected peaks were present, and they were orders of magnitude larger than the baseline noise and unexplainable frequencies.

Future research regarding onboard strain measurements in model scale Francis turbines should first focus on capturing the mean strain values despite temperature drift, either through compensation or extra procedures during the measurements, or in the post-processing. From there, the foundation for a numerical model or tool to estimate the life time reduction based on operation schemes as the input can be made. This foundation can be further expanded upon and generalised with more measurements of a similar fashion on other runner designs of various specific speeds.

Keywords: Francis turbines, Flexible operation, Off-design conditions, Runner fatigue, Onboard measurements, Strain gauge

Sammendrag

Med de planlagte utslippskuttene vil mer av den elektriske energien måtte komme fra fornybare energikilder. To av de største potensielle kildene er vind- og solenergi, enskjønt de har den ulempen at de også er periodiske og ikke-regulerbare. Siden elektrisitetsproduksjonen til en hver tid må samsvare med forbruket må andre energiprodusenter i samme strømnett øke sin fleksibilitet for å kompensere, noe vannkraft er meget godt egnet til å gjøre. Men med hyppigere start-stopp-sykluser og raske lastendringer kan man forvente en økning i materialtretthet og havari på reaksjonsturbiner, slik som Francis-turbiner, så det å kunne forutsi hvor mye ekstra skade dette nye driftsmønsteret vil forårsake er av høy interesse.

Hovedmålet for oppgaven er å forbedre forståelsen av hvordan ulike driftspunkter og mønster påvirker Francisturbiner gjennom modellforsøk med ombordmålinger av tøyning der løpehjulsblader er mest utsatt for sprekkdannelser.

Fokusert på å presentere både et eksperimentelt oppsett og funnene, dykker denne studien inn i en omfattende målekampanje fokusert på en Francisturbin med lav spesifikk hastighet. Disse eksperimentene utgjør en kritisk del av HydroFlex-prosjektet, som ønsker å validere simuleringer og få en dypere innsikt i den reduserte levetiden til Francisturbiner som tilskrives økt utmattingsbelastning som følge av fleksibel drift.

Et oppsett og prosedyre for kalibrering av strekklapper er utviklet, og resultatene presenteres sammen med forslag til ytterligere forbedringer. Dette kalibrering-soppsettet består av både en skreddersydd jigg for nøyaktig og repeterbar belastning av løpebladet på en forutsigbar måte, og en nummerisk model i ANSYS Mechanical med de samme grensebetingelsene for å simulere spenningen og tøyningen ved plasseringen av strekklappene under de samme belastningene.

Ombordmåling av bladtøyningen under drift i en modell Francisturbin testrigg ved Vannkraftlaboratoriet (NTNU) presenteres også med både noen av utfordringene man har møtt og også de endelige resultatene som er oppnådd. Målingene spenner over et bredt spekter av farts- (n_{ED}) og strømningsfaktorer (Q_{ED}), og viser virkningen av disse på den resulterende dynamiske belastningen.

Sentrale utfordringer har vært lav følsomhet og lite utslag i strekklappene som først ble brukt, og en stor mengde elektrisk støy i målekjeden. Høy sensitivitet for selv små endringer i vanntemperaturen har også vært en stor utfordring, noe som har gjort at den målte gjennomsnittlige belastningen driftet langt fra sin kalibrerte verdi for samme belastning. Forbedringer av strekklappoppsettet og forslag til hvordan man kan beregne gjennomsnittlige trender i tøyningen til tross for temperaturdrift diskuteres.

Resultatene viser at mens topp-til-topp-tøyningen øker når belastningen økes over designpunktet, oppstår likevel den høyeste topp-til-topp ved dellast. Det er også sett hvordan avløpskanten påvirkes forskjellig nær navet kontra ringen ved driftsforhold utenfor optimalt driftspunkt, dette på grunn av hvilke effekter som er hovedkilden til vibrasjonene på de to ulike plassene. Gyldigheten til resultatene ble også styrket av FFT-analysen av den målte tøyningen, da alle de forventede toppene var tilstede, og de var flere størrelsesordener høyere enn den generelle støyen og uforklarlige frekvensertopper.

Fremtidig forskning angående tøyningsmålinger ombord i modellskala Francisturbiner bør først fokusere på å fange opp gjennomsnittlige tøyningsverdier til tross for temperaturdrift, enten gjennom kalibrering, ekstra prosedyrer under målingene, eller i databehandlingen i etterkant. Derfra er grunnlaget lagt for en numerisk modell eller et verktøy som estimerer levetidsreduksjonen basert på driftsmønster som input. Dette grunnlaget kan utvides ytterligere og generaliseres med flere målinger på lignende måte med andre løperhjul av forskjellige spesifikke hastigheter.

Nøkkelord: Francisturbiner, Fleksibel drift, Ugunstige driftsforhold, Løpehjul-stretthet, Ombordmålinger, Strekklappmålinger

Acknowledgements

First of all, I would like to thank my supervisor Ole Gunnar Dahlhaug for not only giving me this opportunity and helping me accomplish something I wouldn't even have dreamed possible ten years ago. Your guidance, support and willingness to take the time I needed throughout both the highs and lows in this proverbial roller coaster have been instrumental and deserves an enormous amount of praise. Also, the contribution from my co-supervisor and friend, Igor Iliev, can not be overstated. From the informal chit chats to insightful discussions throughout have truly helped me in lifting the quality of my work to a whole other level, and your eagerness to respond to all my silly questions have really been both essential and inspiring. This process would have been a lot more of an uphill battle without your support, and for that I am truly grateful. I also want to thank Bjørn Winther Solemslie who's shared of his vast knowledge and experiences in experimental work, data processing and the field of science in general, and spent valuable time with me in discussions. Whenever I've had a challenge or uncertainties in my endeavours, you've had a solution or idea ready at hand. And your *open door* mentality to anyone and everyone during all my time at the Waterpower Laboratory have been encouraging, and something I aspire to bring with me in my future ventures.

Secondly, I want to say that I've been really fortunate with my colleagues, the scientific- and technical staff, fellow PhD candidates, Post-docs, and master students here at the Waterpower Laboratory through these past four years. You guys have truly made the working environment something out of the ordinary, and while you are too many to mention you all know who you are. Thank you all! A special thanks is however warranted to my office mates, Helene and Nirmal. Throughout you have helped keep my spirits up, and our sometimes long and off topic discussions have been a welcome distraction. Thanks guys! Also, none of the lab activities would have been possible without all of the technical staff, but I am especially grateful

Contents

II Papers 49

List of Tables

List of Figures

List of Symbols

Latin Symbols

b_1	Runner inlet height	m
c_2	Outlet flow relative velocity	m/s
c_{m2}	Outlet flow relative meridional velocity component	m/s
c_{u2}	Outlet flow relative rotational velocity component	m/s
d_1	Runner inlet diameter	m
d_2	Runner outlet diameter	m
E	Young's modulus of elasticity	MPa
f_n	Runner rotational frequency	Hz
f	Frequency	Hz
$f_{r,RSI}$	Rotating blade passing frequency	Hz
$f_{s,RSI}$	Stationary blade passing frequency	Hz
GV	Guide vane angle	deg
H	Head	mWc
H	Head	m
H_{max}	Max head	mWc

H_{max}	Max head	m
k	Harmonic number	$-$
L	Length	m
m	Harmonic number	$-$
$ND\#$	Specific nodal diameter $(0, 1, 2, ...)$	$-$
n_{ED}	Speed factor	$-$
Q_{ED}	Discharge factor	$-$
R	Electrical resistance	Ω
Q	Flow rate	m^3/s
R_g	Strain gauge resistance	Ω
t	Time	s
u_2	Runner outlet tangential velocity	m/s
v_2	Outlet flow absolute velocity	m/s
V_{ex}	Bridge excitation voltage	V
V_o	Bridge ballance voltage	V
V	Electrical potential	V
Z_r	Number of runner blades	$-$
Z_s	Number of guide vanes	$-$

Greek Symbols

β_2	Outlet flow angle	$^{\circ}$
Δ	Change in quantity	$-$
$\mu\varepsilon$	Micro strain	$\mu m/m$
ν	Nodal diameter	$-$

ε	Strain	m/m
σ	Stress	MPa

Abbreviation

BEP   Best efficiency point

F-101   Francis 101

FDB   Flow Design Bureau

FFT   Fast Fourier transform

GF   Gauge factor

MTBF   Mean time between failure

RSI   Rotor-stator interaction

RVR   Rotating vortex rope

$Sh\#$ Strain gauge, hub side

$Sref$ Strain gauge, unstrained reference

$Ss\#$ Strain gauge, shroud side

VKL   Waterpower Laboratory/Vannkraftlaboratoriet

Part I

Summary

Chapter I

Introduction

■ In this chapter we introduce the topic at hand and give some background information, followed by a summary of the objectives, activities, and research contributions.

1.1 Motivation

With the month of July 2023 being the warmest month ever on record at the time of writing [1] and the deadlines for making significant cuts in the emission of CO_2 approaching fast, fairly major changes in the production of electric energy needs to be done in the coming years. The European Union has committed itself to reduce the emission of CO_2 and cut down on the reliance on fossil fuels. The stated goal is that at least 32% of the electrical energy production within the EU must come from renewable sources by 2030, and in the longer term the goal is to increase this to 80% by 2050 [2, 3]. In order to meet the demand for electrical energy while at the same time reducing emissions within the time frame, renewable energy sources such as solar- and wind power is the most likely candidates to fill the need. However, both solar- and wind power are intermittent and non-dispatchable sources meaning that they will generate the obtainable power from their source with little regard to the demand that is put on the grid. Since the energy production must match the consumption at all times the grid must be balanced, meaning that having a more significant fraction of non-dispatchable sources on the grid also puts a greater demand for regulating the power output from other sources in the grid to maintain stability [4].

As a renewable and highly dispatchable energy source, hydropower is uniquely positioned to assist in the transition towards a low emission and renewable energy

mix. With 87% the electric energy production in Norway originating from hydro-power [5] and increasingly extensive interconnectivity between the Nordic- and continental European grids, Norway is well positioned to assist in this transition by providing flexibility in energy production. The most commonly used turbine in Norwegian hydropower plants is the Francis turbine [6]. The Francis turbine is a fully submerged reaction turbine with a radial inflow and an axial outflow, named after its inventor James Bicheno Francis.
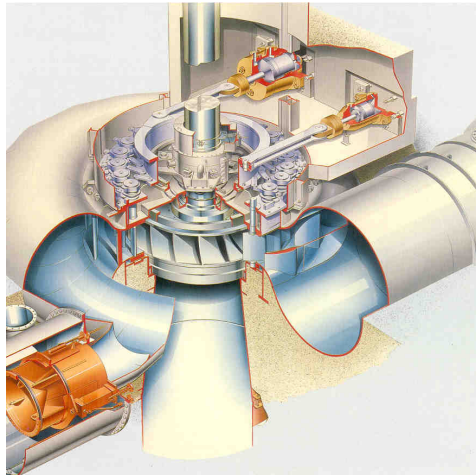
Figure 1.1: Illustration of a typical Francis turbine [Kværner Brug AS]

The Francis turbine has a very high peak efficiency and can be designed for a wide range of both discharge and head, more so than any other type of commonly used hydropower turbine. One drawback of operating Francis turbines, or any other reaction turbine, in a wider range of power outputs and with a more rapid ramping or load variation and frequent start-stop cycles is that they typically experience more fatigue loading and damage. An increase in fatigue loading may drastically shorten the mean time between failures (MTBF), especially for older units and turbines designed for a more stable operation scheme. Meaning that a better understanding of how more flexible operation affects the lifespan of the turbine and runner, and what possible changes in the design philosophy could be used for new designs is of high interest.

1.2   Background

The work behind this thesis and the included papers has been conducted as a part of the international and multidisciplinary research project HydroFlex. HydroFlex was

funded by the European Commission through Horizon 2020 [7]. Within HydroFlex, the work presented in this thesis was a part of work package 3 (WP3), focusing on the *Flexibility of turbines*, specifically Francis turbines. The main goal of WP3 was to create a tool for lifetime estimation of turbines, and develop a new design methodology or guidelines for new turbines that are expected to operate with a higher degree of flexibility. The focus of this work has been to perform onboard strain measurements in a model Francis runner to provide data for validation of numerical simulations.

The biggest challenge at hand was getting reliable data from strain gauges mounted in the model runner, something of which has been attempted in various projects at the Waterpower Laboratory, NTNU, going back to 2006-07 [8]. One of the main issues is the forces acting on the runner during operation being relatively low, while at same time, the runner blade material has to be suitable for the task and stiff enough to be structurally sound. Another issue during previous attempts has been the design of the runner used and how it was assembled and held together. While similar experiments have been done several times at other institutions on model turbines of a similar scale, a common theme is that these experiments are done in cooperation with turbine manufacturers, meaning that confidentiality comes into the picture and little to no data is made publicly available.

1.3 Objective and activities

The main goal for the experimental work for this thesis was to get a better understanding of how a flexible operation of Francis turbines affects the fatigue loading of the blades. While this has been done before on both model [9, 10, 11] and prototype [12] runners, it is still a challenge to quantify the cost of flexible operation schemes. Another point was that it was not fully known how behaviours and trends seen on a prototype would scale down to the model scale due to factors such as material properties which are not scalable. Finally, it was of interest to measure and collect data, make experimental procedures, and share experiences openly to help others who might want to perform similar types of measurements, both at the Waterpower Laboratory and elsewhere.

During the work behind this thesis, a new hybrid calibration procedure for strain gauges was developed, and some iterations on the measurement chain and strain gauges were performed to get reliable and believable strain data. Both calibration of blade strain and several iterations of the experiment and setup were performed at the Waterpower Laboratory. There were several technical challenges along the way, ranging from transmitting data from a rotating frame of reference to the stationary,

to how to keep electronic equipment dry and safe from water. As a result, some of the initial goals and expected results set by the author of this thesis could not be met, such as onboard pressure measurements and absolute strain data for validation. However, offset strain values were recorded and analysed successfully. Some ideas and proposals on changes in the experiment procedure and post processing, such as getting an estimate on the mean change in strain from a known baseline, will be presented.

Research contributions

- Hybrid calibration method where a combination of relatively simple numerical simulations and an identical physical setup can be used to reduce uncertainty in the measured strain.

    – *With better temperature control during calibration, a temperature dependent calibration component might be acquired as well.*

- Design of a tailor-made low specific speed Francis runner used in onboard strain gauge experiments.

- Unique strain gauge data from a wide range of operating conditions on a model Francis turbine and the evaluation of the measured data.

—————————Chapter II—————————

Theoretical background

■ This chapter will present the theory behind how the measurements of strain is done and what strain is, before moving on to describing some of the most important flow phenomena in the turbine during operation.

2.1 Measurement of deformation

Strain gauges

When a force is acting upon a solid element a slight deformation of the element will occur, and this deformation is called strain. Strain is measured in the deformation length or distance relative to the original and unstrained length, or $\Delta l/l_0$ [m/m]. As long as the deformation is elastic and not too close to the upper limit of elasticity, the amount of strain will be proportional to the applied force for most materials [13]. Since strain can be indicative of the stresses in a structure or element and excessive stress, or stress cycles, can lead to fatigue and failure. Excessive strain can also be an early warning of impending failure of a structure[14], so it is of high interest for engineers to measure the strain at crucial points and areas. As an example, if an elastic rod is stressed in one direction the strain can be calculated with Hooke's law, and thus, stress can be calculated from the strain. Hooke's law simply states that the stress of an element is proportional with the strain and the material elasticity, or:

$$\sigma = E \cdot \varepsilon \tag{2.1}$$

where ε is the strain, E is Young's modulus and is specific for the material in the rod, and σ is the stress in the rod. This relationship gets more complicated if the element is stressed in more than one direction, but they are still coupled. One

reliable and inexpensive way to measure stress and/or strain is through the use of strain gauges. Strain gauges are in essence long and thin conductive wires, and as the wire is stretched or compressed the resistance in it will change accordingly. The resistance in conductive wires are proportionally dependent on their length, inversely proportional to their cross sectional area, and of course the resistive properties of the material used. As a result, the change in resistance in a strain gauge is approximately directly proportional to the change in its wire length. A slight deviation from this ideal relationship comes from the fact that as the wire is stretched, the cross section will contract some. The amount of contraction depends on the Poisson's ratio of the material used, and this deviation from the ideal isn't too significant, but still measurable. As a side note, the resistance of conductive materials will also depend on the temperature. While strain can be measured by stretching out a wire along the length of the element to be measured on, it is most common to run the wire back and forth on a small backing to concentrate the area of which the measurements will be done on [15].

Wheatstone bridge

Usually, elastic strain is in order of magnitude of $\sim 10^{-3}$m/m or lower, meaning that the change in resistance will be equally low. Because of the small scale of the resistance change, measuring it directly is impractical and inaccurate. To overcome this limitation, a Wheatstone bridge can be utilised (Figure 2.1). The working principle of a Wheatstone bridge is that a voltage is applied to a parallel circuit. In each of the parallels there are two resistances in series, i.e. four all together. If the resistances are equal, there will be no potential difference between the midpoints of the two circuits and the bridge is balanced. However, if strain is applied to the strain gauge (R_3), the resistance will change. This unbalance will lead to a difference in the potential between the two circuits and can be measured accurately even with small changes in resistance [15]. If one strain gauge is used in a Wheatstone bridge, it is said to be in a quarter bridge configuration. For simpler structures where the strain can be expected to be equal but in opposite directions on two locations, such as both sides of a plate, two strain gauges can be wired in series (i.e. R_2 and R_3) to double the output of the measurement, and this configuration is often referred to as a half bridge. If the structure permits and the strain is guaranteed to only go in one direction, two more strain gauges can be mounted normal to the strain (i.e. not getting affected by it) in place of R_1 and R_4 as a means to automatically compensate for temperature changes in the structure which would otherwise affect the balance of the bridge.
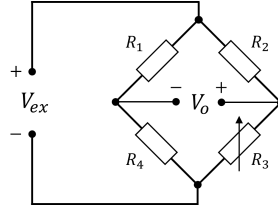
Figure 2.1: Illustration of a Wheatstone bridge with a strain gauge in place of resistance R_3

2.2   Francis turbine flow phenomena

There are several flow phenomena inside a Francis turbine which causes both local and global pressure pulsations. These pulsations will of course also induce vibrations on the structures within the turbine, and particularly on the trailing edge of runner blades, which have been prone to fatigue damage and failure in the past [16, 17]. Note that this section is not an exhaustive and complete description of all the phenomena that can occur, but the select few that were prominent in the onboard measurements. There are many factors influencing how severe the different off-design phenomena can become, be it turbine design, specific speed, water way dynamics etc.

Rotor-stator interaction

While some phenomena originates upstream of the runner outlet, such as rotor-stator interaction (RSI) between the stationary guide vane cascade and the rotating runner blades at the inlet, the pulsations will still propagate down through the runner blade channels and influence the trailing edge. The cause of the RSI is the non-uniform flow pattern leaving the guide vane cascade, leading to each runner blade channel experiencing a pulsating flow velocity and pressure as they move past each guide vane channel [18]. In an effort to reduce the chance of severe pulsations, vibrations or even resonance, some care is usually taken when designing a turbine by ensuring that the number of runner blades and guide vanes are different. Preferably also with few or no common factors to greatly reduce the chance of resonance. However, the RSI frequency seen in the stationary domain is calculated by:

$$f_{s,RSI} = f_n \cdot Z_r \cdot k, (k = 1, 2, 3...) \tag{2.2}$$

Here, $f_{s,RSI}$ is the RSI frequency, f_n the runner rotational frequency in revolutions per second, Z_r the number of runner blades and k the harmonic number. Equally,

in the rotating domain, the *experienced* RSI frequency is given by:

$$f_{r,RSI} = f_n \cdot Z_s \cdot m, (m = 1, 2, 3, ...) \tag{2.3}$$

Now, $f_{r,RSI}$ is the RSI frequency seen in the runner, Z_s is the number of guide vanes and m is the harmonic number. When measuring the pressure or blade strain, it is to be expected that $f_{s,RSI}$ and/or $f_{r,RSI}$ will be present to some extent, especially for lower specific speed Francis turbines due to the design and the runner inlets proximity to the guide vane cascade outlet. The connection between these two frequencies will be the nodal diameter of excitation. Meaning that:

$$Z_s \cdot m + \nu = Z_r \cdot k, (\nu = ..., -2, -1, 0, 1, 2, ...) \tag{2.4}$$

where ν is the nodal diameter and its sign indicates whether the mode shape rotates with or against the runner rotation [19]. Using equation 2.4 for the turbine used in the current study, assuming only nodal diameters of 5 and lower will be significant enough, two different nodal diameters are found. From equation 2.4, all the excited nodal diameters can be calculated, and for the first six harmonic numbers of both m and k we get the following table:

Table 2.1: Matrix of the excited nodal diameters for the F101 in the test rig at the Waterpower Laboratory with nodal diameters of 5 and lower highlighted.

		m					
		1	2	3	4	5	6
	1	-11	-39	-67	-95	-123	-151
	2	6	-22	-50	-78	-106	-134
k	3	23	**-5**	-33	-61	-89	-117
	4	40	12	-16	-44	-72	-100
	5	57	29	**1**	-27	-55	-83
	6	74	46	18	-10	-38	-66

This matrix can obviously be expanded in both directions to include more nodal diameters, but as higher harmonics will carry lower energy, any resulting vibrations will more be easily dampened and end up being harmless. The first highlighted nodal diameter is $ND5$, and comes from the second harmonic, or $m = 2$ and $k = 3$ (Figure 2.2), the other is $ND1$ and comes from the third harmonic, or $m = 3$ and $k = 4$ (Figure 2.3). Both figures shows the intersection between the blade channels and the inlet pressure harmonics. There is also an excitation of the ND6 from the

first harmonic, but typically higher nodal diameters are less potent and thus also less dangerous. These calculations will give an indication of which nodal diameters that can be excited by the flow, but nothing about which frequencies and nodal diameters the runner itself is susceptible for. However, they will still give a good indication of what to look out for when doing calculations for the runner eigenfrequencies. Though neither show any significant contribution in the measurements, and they are in fact far from the critical frequencies of the runner.
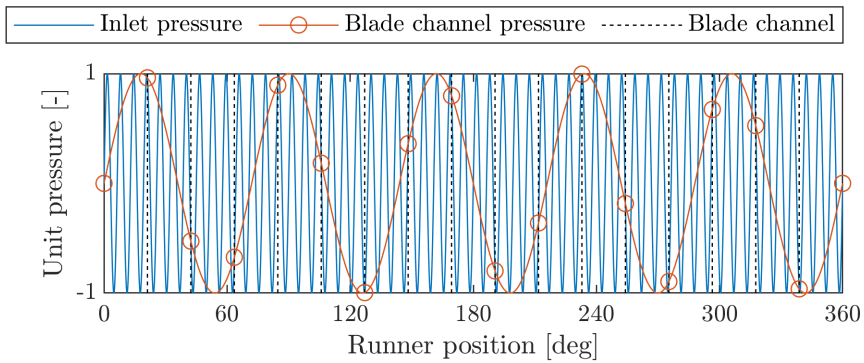
Figure 2.2: Illustration of the ND5 excitation from the second harmonic frequency of the guide vane cascade.
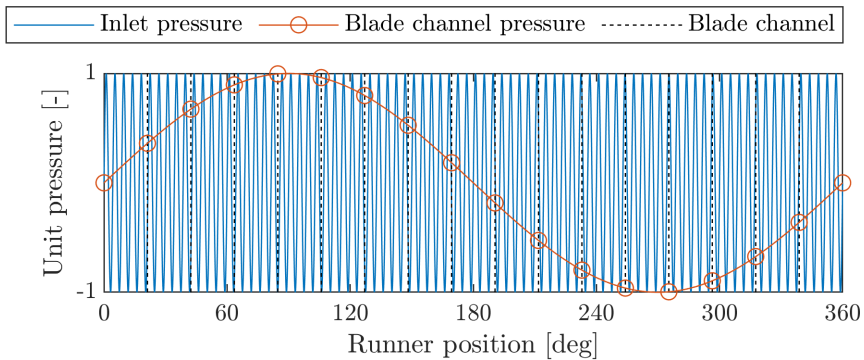
Figure 2.3: Illustration of the ND1 excitation from the third harmonic frequency of the guide vane cascade.
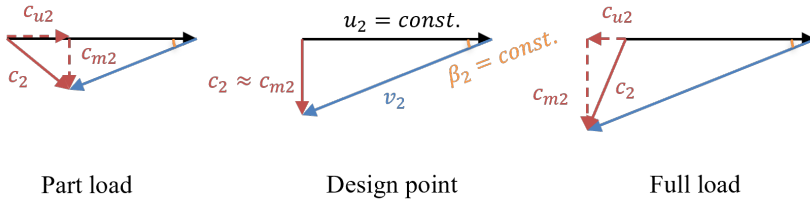
Figure 2.4: Illustration of the velocity triangle at the runner outlet for three different discharges

Rotating vortex rope

In a Francis turbine the outlet angle of its runner blades are fixed and dimensioned for a specific discharge. When operating at, or close to, the design discharge (i.e. BEP) the circumferential velocity in the flow will be small. Since Francis turbines almost exclusively spin their runners at a fixed rotational velocity [20], a change in the discharge will cause a swirl in the exiting discharge. Figure 2.4 illustrates the direction of the swirl based on the change in flow rate. As long as the swirl is low enough, the exiting flow will fill the entire cross section of the draft tube, but after reaching a certain threshold a flow separation will occur and a core of dead or separated water will appear. As the swirl increases, the stagnation point of this core will move upstream until it reaches the hub of the runner. At the interface between the two flow regions, starting from the runner hub, one or more helically shaped vorteces will appear when operating at part load (<BEP), with the number of vorteces depending on the flow conditions and swirl rate. This vortex phenomena is often referred to as a rotating vortex rope (RVR) and it (or they) will not be stationary in the draft tube, but rotate around the stationary core [19]. The rotational frequency of the RVR will vary depending on the discharge and swirl rate. At the higher end of part load ($\sim 50\%$ to $\sim 85\%$ of BEP), a single vortex rope will be present and will typically have a rotational frequency in the range of $0, 2$ to $0, 4$ times the runner rotational frequency [21, 22]. The relative frequency of the RVR is often referred to as *Rheingan's frequency*. As the vortex rope has a pressure gradient around it, there will also be a rotating pressure field in the draft tube. This is most often measured with a couple of pressure transducers mounted on the draft tube wall. When measuring from onboard the runner, the frequency of the vortex rope will be different, as both the runner and RVR is rotating at different velocities. Since the runner is rotating faster, the point of measurement on a blade for instance will have to catch up with the vortex, so if for example the Rheingan frequency is
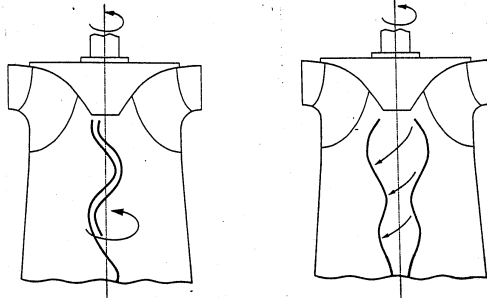
Figure 2.5: Illustration of the rotating vortex rope in the draft tube (right) and a full load vortex (left) [23].

$f_n \cdot 1/3$ the runner will have to complete three revolutions for the vortex to complete one. Measured onboard, the relative frequency of the vortex would then end up being $f_n \cdot 2/3$ since the measurement point would end up passing the RVR twice in those three revolutions, which can also be observed from the measurements later in chapter 5. Note that the measured Rheingans frequency was not $f_n \cdot 1/3$, but relatively close.

Flow asymmetries

Another common pulsation frequency seen in Francis turbines is the rotational frequency itself. There can be many causes of this, but generally speaking it may stem from unbalance in the runner, asymmetrical flows through and out of the spiral casing or the draft tube and its bend [19]. Usually, more severe cases of pulsations from these sources are mostly due to poor or older designs, and thus not necessarily an issue in all turbines, as opposed to the RVR for instance. However, observing the rotational frequency in measurements taken onboard the runner can give some credibility to the measured data, as it is to be expected to be present to some extent.

Useful factors

Often when dealing with measurements, especially on the model scale, some dimensionless factors are used, first of which is the speed factor or n_{ED}:

$$n_{ED} = \frac{n \cdot d_2}{60 \cdot \sqrt{H \cdot g}} \tag{2.5}$$

here we have the rotational speed n, runner outlet diameter d_2, head H and the gravitational acceleration g. Another much used factor is the discharge factor or

Q_{ED}:

$$Q_{ED} = \frac{Q}{d_2^2 \cdot \sqrt{H \cdot g}} \tag{2.6}$$

where the flow rate Q, runner outlet diameter, head and the gravitational acceleration is used.

For reference, the hydraulic efficiency is calculated as shown in equation 2.7

$$\eta = \frac{P_{mech}}{Phyd} = \frac{\omega \cdot \tau}{\rho \cdot g \cdot H \cdot Q} \tag{2.7}$$

η is the hydraulic efficiency and is the ratio between the mechanical power output P_{mech} and the hydraulic power input P_{hyd}. ω is the angular velocity τ is the shaft torque. ρ is the water density, g is the gravitational acceleration, H is the head and Q is the flow rate.

──────────────── **Chapter III** ────────────────

Experimental setup

■ This chapter attempts to give an overview of the different phases of the experiment, starting with calibration and preparation, to post-processing and data analyses methods used.

3.1 Calibration and strain gauges

Strain gauge and gauge factor

Strain gauge manufacturers will often present the sensitivity of strain gauges as the gauge factor (GF). The GF is a ratio of the change in resistance to the change in length, or strain.

$$GF = \frac{\frac{\Delta R}{R_0}}{\frac{\Delta L}{L_0}} \tag{3.1}$$

$\frac{\Delta R}{R_0}$ is the change in resistance over the nominal resistance at rest, and $\frac{\Delta L}{L_0}$ is the change in length over the nominal length at rest, i.e. strain and often also expressed as ε. Looking back at the Wheatstone bridge in Figure 2.1, the voltage difference between the two parallel circuits can be calculated using Ohm's law. Expanded and rearranged it becomes:

$$V_o = \frac{R_3 \cdot V_{ex}}{R_2 + R_3} - \frac{R_4 \cdot V_{ex}}{R_1 + R_4} \tag{3.2}$$

where V_o is the voltage difference and V_{ex} is the voltage applied to the bridge, also referred to as the excitation voltage. Looking at a quarter bridge configuration where R_3 is functioning as the strain gauge (R_g), and assuming that the remaining

bridge resistances are the same, the equation can be rearranged and simplified to:

$$V_o = V_{ex} \cdot \frac{R_g \cdot R - R^2}{(R_g + R) \cdot (2R)} \tag{3.3}$$

If we then express the strain gauge resistance as the sum of the nominal resistance (R) and the difference from the nominal resistance, or $\Delta R + R$, or even use the ratio of change in resistance to nominal resistance, as in Equation 3.1.

$$V_o = V_{ex} \cdot \frac{\frac{\Delta R}{R} \cdot R^2 + R^2 - R^2}{(\frac{\Delta R}{R} \cdot R + 2R) \cdot 2R} \tag{3.4}$$

Simplifying further, and we get

$$\frac{V_o}{V_{ex}} = \frac{\frac{\Delta R}{R}}{2(\frac{\Delta R}{R} + 2)} \tag{3.5}$$

Finally, we can rearrange it to get an expression for $\frac{\Delta R}{R}$ and combine it with Equation 3.1

$$\varepsilon = \frac{4}{\frac{1}{V_o/V_{ex}} - 2} \cdot \frac{1}{GF} \tag{3.6}$$

With this, the applied strain can be calculated assuming all the resistors and the nominal strain gauge resistance is the same, and no defects in the bonding between the strain gauge and strained element. To account for differences in resistances and the bonding, a more thorough calibration of the strain gauge can be done. Another thing to note from Equation 3.6 is that the gauge factor is what's giving the sensitivity of a strain gauge, where a higher GF will give a higher sensitivity. Usually, the equipment used to measure the bridge response have a fixed range it can work within, so this and the GF should be taken into account when deciding on which strain gauge that should be used for an application if the expected range of strain is known or at least can be estimated.

Calibrator fixture

At an early stage in the project behind this thesis, it was decided that a calibration of the blade mounted strain gauges should be done in order to reduce uncertainties regarding the strain measurements. To accomplish this, a special blade fixture was designed and made, seen in Figure 3.1, and a numerical setup with the same boundary conditions was replicated in ANSYS Mechanical. The blade is secured onto the fixture using the bolt bores situated on the hub section of the blade.
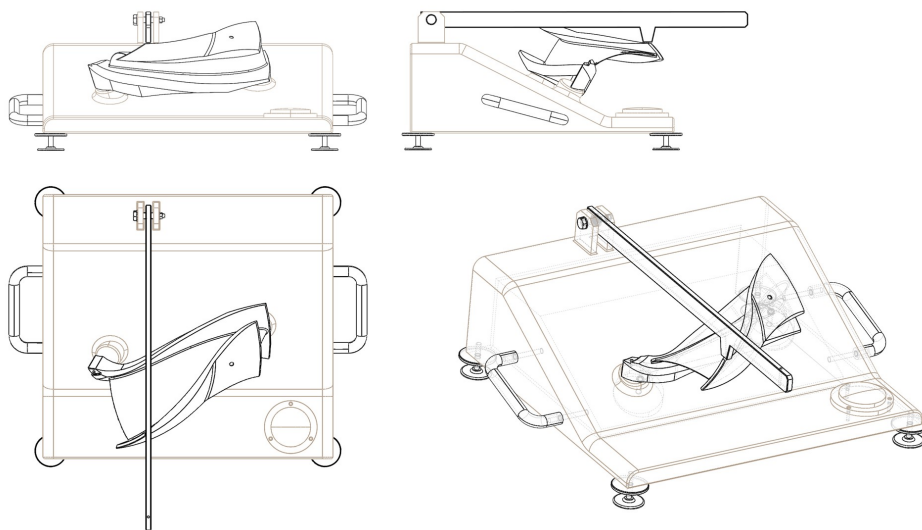
Figure 3.1: Blade fixture to calibrate the instrumented blades, [27]

Meanwhile, the loads are exerted on the shroud section. The blade is oriented so that the surface normal at the load application point is aligned vertically. The fixture body is deliberately over-engineered to provide ample stiffness and stability during calibration. For ease of handling in the laboratory, it's fabricated from 7075 Aluminium Alloy to minimise its weight. The pivot arm, composed of S355 Non-Alloy Steel, is mounted to the primary body via a low-friction SKF 607-2RSL sealed ball bearing. The material selection for both components prioritises a slightly higher strength and marginally lower hardness compared to the blade material, which is JM7-15 Aluminium Bronze. The surface area of the contact point between the blade and the arm was set to be as small as possible, yet large enough that plastic deformation occurs. Under typical operating conditions of the model runner, the maximum principal elastic strains close to the blade trailing edges are nearly parallel to the edge itself. This was validated through initial high-fidelity simulations conducted as part of the HydroFlex project, and this phenomenon appears consistent in other Francis turbines as well [24, 25, 26]. Thus, uni-directional strain gauges were oriented parallel to the trailing edge near to, but not on, the trailing edge chamfer.

For the calibration procedure, the amplified signal was measured and recorded using a NI LabVIEW program and NI cDAQ module. The calibration was done over 10

steps, each step repeated four times, and the weights were applied in succession from minimum to maximum, then reversed by taking them off in succession from maximum to minimum, and then repeated again. This was done in order to both check the repeatability of the calibration by having each point measured several times, and to capture the hysteresis due to how many types of measurements will have an offset from the ideal mean dependent which direction the input change comes from.

3.2   HydroFlex runner and turbine test rig
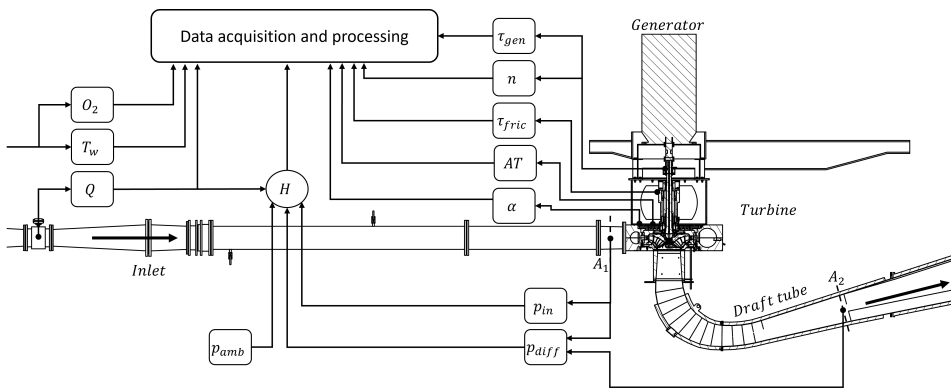
Figure 3.2: Overview of the turbine test rig used in the experiment [28].

A new model Francis runner was designed and made for the experiments called Francis-101 (F-101). The runner was dimensionally constrained by the existing test rig at the Waterpower Laboratory, i.e. runner diameters, labyrinth seals, rotational direction, etc. The test rig itself is IEC60193 [29] compliant and was made for a series of model tests performed in 2006 in relation to the low specific speed turbine designed for Tokke power plant [30, 31] and has been used and simulated for the Francis 99 workshops [32]. The design condition of the F-101 runner is near the speed factor (n_{ED}) of 0,18 and with the best efficiency point (BEP) close to a guide vane opening angle of $10°$. The runner design was accomplished using a fully quadratic response surface model first developed at the Waterpower Laboratory during Igor Iliev's doctoral studies [33] within the HydroCen project [34]. Of the original 15 free parameters used by the model, three were fixed for the specific requirements of the F101 runner and its usecase [35]. Firstly, the trailing edge (TE) was positioned so that the entire length of the blade is fixed within and fully constrained by the hub- and shroud sections. Second, the blade profile thickness was set to be as thin as possible to mitigate the stiffness of the blade material and

maximise the response from to the forces involved in the model turbine during operation. Finally the TE was made radial and with no leaning to reduce the blade shape complexity when machining them. The remaining 12 parameters were obtained through the model with the criteria of maximising the hydraulic efficiency of the runner, a more detailed description can be found in Paper 4 [36] or the PhD thesis of Igor Iliev [33]. In total 21 runner blades were manufactured, with the extra intended for instrumentation, both for this project and future experiments.

Table 3.1: Main model runner dimensions

Parameters	Symbol	Value	Unit
Runner inlet diameter	d_1	620	mm
Runner inlet height	b_1	59,6	mm
Runner outlet diameter	d_2	349	mm
Runner blades	Z_r	17	
Rated head	H	14	mWc
Max head	H_{max}	30	mWc
Flow rate	Q	69 - 334	l/s
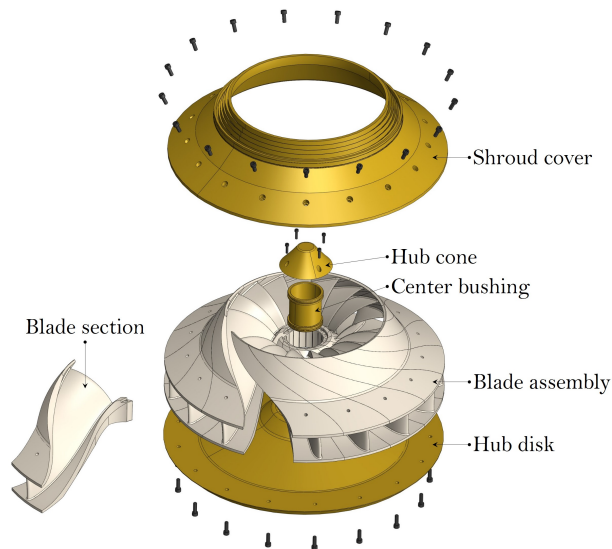
Figure 3.3: Exploded view of the F-101 runner assembly, [27]

3.3   Equipment

Onboard equipment

Strain gauges

The first set of strain gauges chosen were HBM 1-LY41-6/350 1 grid linear strain gauges [37]. They were assumed to be suitable due to their small size, appropriate nominal resistance, and similar thermal expansion properties to the runner blade material. It was hoped that this would allow for a stable enough signal without any significant drift caused by temperature changes, and that the small response could still be amplified and recorded.

After the resistive strain gauges and measurement setup were found inadequate, shown in Paper 3 [28], semiconductor strain gauges were chosen as a replacement. The new strain gauges were Kulite S/UDP-350-175 linear strain gauges [38]. They were closely matching the resistive strain gauges in terms of size, but had a gauge factor of more than 50 times that of the HBM strain gauges.

Table 3.2: Comparison between the two types of strain gauges used

	HBM 1-LY41-6/350	Kulite S/UDP-350-175
Grid material	Resistive metal foil	Semi-conductor
Active length	6mm	$3,56$mm
Gauge width	$2,8$mm	$0,41$mm
Gauge factor	$2,11$	115
Nominal resistance	350Ω	350Ω

Note that with the more sensitive strain gauges installed, temperature adjustment over the course of the measurement campaign would be needed. During mounting of the Kulite strain gauges, it was found that the resistance was at the upper limit given by Kulite, deviating from the nominal resistance (350Ω) by as much as 70Ω. This deviation allowed for the continued use of the already acquired foil resistors, and instead wire an adjustable resistance in series to get the appropriate resistance.

Amplifiers

To amplify the signal from the strain gauges, ICA3H from Mantracourt [39] was used. They were deemed a suitable option with all the constrains. Firstly, they were initially mounted inside the center bushing inside the hub of the runner (see Figure 3.3), so size was an important matter. Secondly, they had an amplified

output of $\pm 10V$ allowing for full utilisation of the range and resolution of the DAQ equipment. Finally, they allowed for adjustability of the amplifier gain after manufacturing and shipping, something of which the other considered options did not have.

Table 3.3: ICA3H amplifier specifications

	Nominal	Range	Units
Supply voltage	± 14	± 1	V
Bridge excitation	5	$\pm 0, 1$	V
Bridge impedance	1000	$-650 \& +4000$	Ω
Bridge sensitivity	$2, 5$	$-2 \& +147, 5$	mV/V
Amplifier gain*	≈ 150	$-147, 5 \& +594$	-
Output voltage	± 10	-	V
Band width	1000	-	Hz
Linearity	$0, 02$	-	%FR

* Calculated from the stated bridge sensitivity

For the first setup iteration, the gain of the amplifiers were essentially set as high as possible due to the low response from the strain gauges during calibration. In the end, it turned out that it had been set slightly above the rated range from Mantracourt, but they still functioned fine during calibration. For the second iteration with more sensitive strain gauges, the gain could be lowered substantially. In the end, it was set to $\sim 86\times$, as that would give us a range from $0V$ to $7V$ when going form no load to max expected loading during operation. With that range, it was still enough headroom for some temperature drift before clipping, and full response in both directions from $0V$. A more detailed description of how the required gain was calculated for the second iteration is presented in Paper 4.

Bridge resistors

To complete the Wheatstone bridge with the strain gauges, three extra resistors had to be wired to each strain gauge. With the first iteration, high precision metal foil resistors of 350Ω were used [40]. For the second iteration, an additional 200Ω Bourns PV36 trimmer potentiometer was wired in series with each of the used foil resistors. They allowed for manual temperature compensation during the course of the experiment. The reasoning behind using potentiometers with a smaller max resistance and wire them in series with a fixed resistance was that a more precise adjustment of the total resistance would be possible, as the adjustment screw would

give smaller changes in resistance per rotation.

Slip ring

A slip ring was used to feed power to-, and transmit signals from the amplifier assembly mounted in in the runner and on the shaft. A Penlink SRH80180-24S was installed on the turbine shaft. This slip ring had 24 channels or leads, enough to transmit all the amplified signals out and power supplied to the amplifiers in.

Hub cone and cable pass through

Due to the construction of the center bushing and the order of which the runner installation in the rig and assembly of the final pieces had to be done, it was impossible to run cables through the wall of the bushing and seal everything up prior to installation in the rig. Given the challenge at hand, and the need to keep the interior of the hub dry due to electronics a new cone was designed and manufactured as well. The cone has an extension with a threaded piece with a conical hole, and a fitting nut with inner flange at one end. During assembly, the wires are put through a hole in a conical rubber plug which fits in the conical hole on the hub cone. When the end nut is screwed on, the flange will push the plug into the hole, tightening up and sealing all around the cables. This solution will of course affect the flow in the draft tube to some extent, but was still regarded as the only viable option with this setup and runner assembly design.
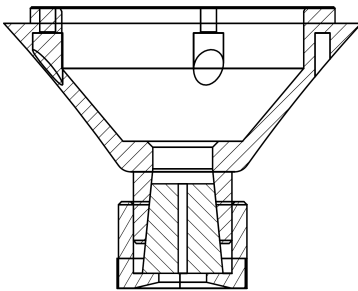
(a) Cross section of the new hub cone with the plug for cable pass through

(b) Closeup of the cone during assembly. *Note that the wires were yet to be tucked close to the cone surface and tied down at this point.*

Figure 3.4: The hub cone assembly used to pass cables from the submerged part of the turbine and into the hub where a cavity is open to the atmosphere through the hollow turbine shaft

Assembly and wiring
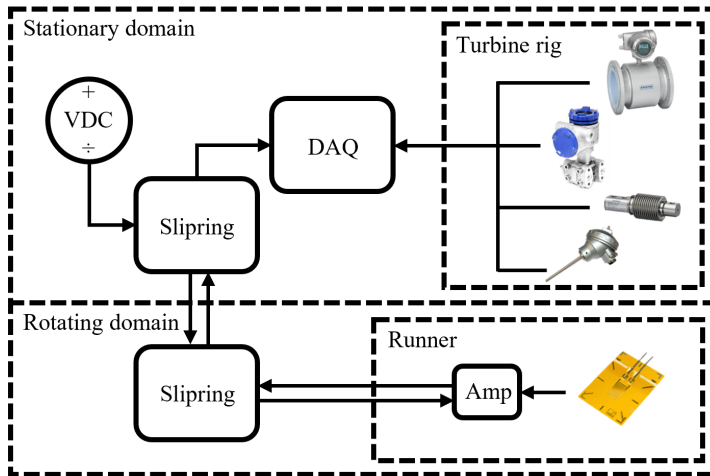
Figure 3.5: Schematic illustration of the measurement chain.

Assembly, first iteration

For the first experiment iteration, the amplifiers and bridge resistors were mounted on 3D printed holders (Figure 3.6) that allowed for them to be pre-wired, tested and stacked outside of the runner hub (Figure 3.7 a), and then simply put in place as one single unit. Each of the holders could have two amplifiers mounted on them, and the bridge resistors was placed right next to each amplifier, simplifying the soldering. In one end of the hub assembly were the wires going up through the turbine shaft centre, also prepared beforehand and kept as one bundle. This wire harness contained both signal wires coming out off- and power supplied to the amplifiers. On the other end of the assembly, small connectors were fixed on the top plate in the stack (Figure 3.7 b) so that the leads coming from the strain gauges could easily be connected to its destined amplifier before sealing the centre bushing and hub. One reason for the placement of the amplifiers inside the hub was proximity to the strain gauges, both in order to keep the wire resistance in that corner of the bridge as low as possible and to reduce the voltage drop of the two leads measuring across the bridge. It was also believed that the amplification should happen before any long wires through the turbine shaft, as electrical noise picked up before the amplifiers would then also be amplified, reducing the signal to noise ratio. The signal cables through the turbine shaft were twisted pairs for each signal, and the power supply wires were shielded.
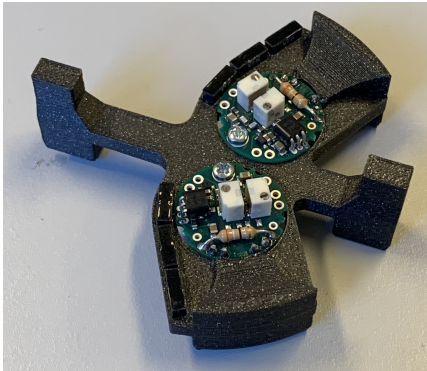
(a) Top view of one amplifier holder containing two amplifiers and six bridge resistors
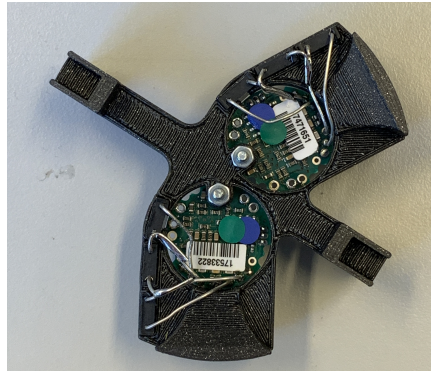
(b) Underside view of one amplifier holder containing two amplifiers and six bridge resistors

Figure 3.6: Closeup of one of three amplifier holders in the first iteration of the amplifier assembly, stacked on top of the others and mounted in the center bushing. Bridge resistances can be seen next to and soldered to toe amplifiers. Two more leads would be soldered on to this and led to the strain gauge connectors.
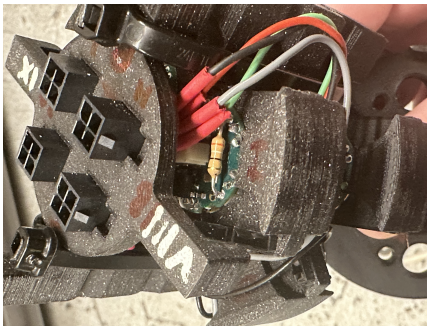
(a) Closeup of the assembled stack
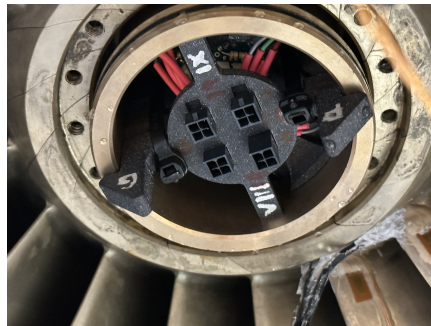
(b) Closeup of the stack inside the runner hub

Figure 3.7: Closeup of the assembled stack and the assembly in the runner hub.

Assembly, second iteration

For the second experiment iteration however, physical access was required to the trimmer potentiometers while the rig was sealed up and filled with water to account for temperature drift. The trimmer potentiometers for all three corners of the bridge, along with their pair of fixed foil resistors, can be seen next to the amplifier in Figure 3.8 a. Therefor the whole amplifier and resistor assembly was redesigned to sit around the turbine shaft, just above the slip ring, as shown in Figure 3.9. As a result, the leads from the strain gauges to the bridge had to be extended through the turbine shaft. However, with the adjustable resistances in the three remaining corners of the bridge, any unbalance from the resistance of the longer wires could easily be balanced out.
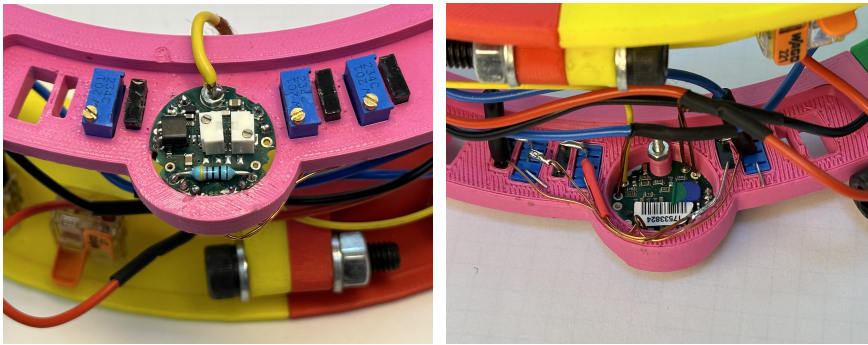
(a) Top view of one amplifier with three bridge resistors

(b) Underside view of one amplifier with three bridge resistors

Figure 3.8: Closeup of the second iteration of the amplifier assembly, intended for turbine shaft mounting

Figure 3.9: The amplifier assembly mounted on the turbine shaft and connected to the slip ring (out of frame)
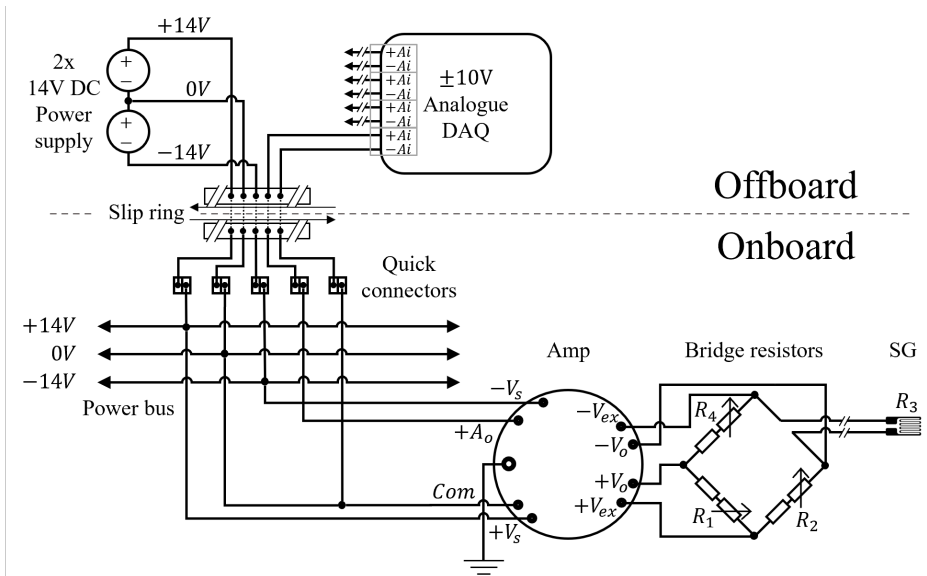
Figure 3.10: Wiring diagram of one strain gauge, bridge and amplifier connection.

While figure 3.10 shows the second iteration with variable potentiometers in the bridge, the first iteration is wired the same but with only fixed bridge resistors. All five strain gauges were wired in the same way but through different channels in the slip ring. The power bus is just three single wires which branches off to each amplifier around or inside the shaft. A full table of slip ring wire colours and pin numbers can be found in the appendix.

3.4 Onboard measurements with strain gauges

Strain gauge location

Four strain gauges were mounted on the trailing edge of two neighbouring blades. The strain gauges were oriented to measure parallel to the trailing edge, and close to the hub and shroud section of each blade. For the second experimental iteration, a fifth strain gauge was mounted inside the hub cone of the runner as an attempt to have an unloaded strain gauge measure only the effects of temperature changes.

Noise and temperature drift

For the first iteration of the experiment, the very low response from the strain gauges compounded with severe electrical noise when the turbine generator was turned

(a) Outlet of the runner   (b) Axial cross section of runner
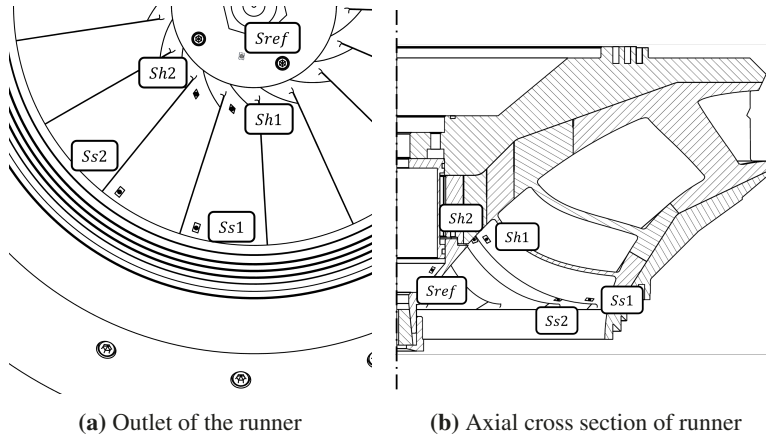
Figure 3.11: Location of the installed strain gauges, note that $Sref$ is mounted on the inside of the runner cone [36].

on and made it difficult to get any useful data. The low response was obviously due to the low gauge factor of the strain gauges, even though there should have been some changes to the mean strain when comparing different load conditions. As for the excessive noise in the signals, it is suspected that the source came from the generator as it would only appear with it turned on. Due to a mistake during final installation in the rig, the mounting hole of the amplifiers were not grounded to the test rig itself. Note that the $0V$ line from the power supplies had to be grounded. During the first round of experiments, no temperature compensation was done, so a slow but steady drift in the mean strain could be seen throughout the measurements which took place over several days. Some measures were taken in an attempt to overcome the issues with temperature drift. Between each measurement series, usually ~ 10 points, a repetition point was measured. This repetition point was chosen to be close to BEP, and more specifically at $n_{ED}0,18$, GV $10°$, and H_n $12,0$m for the first iteration and H_n $12,3$m for the second. The point itself was somewhat arbitrarily chosen, but set to a operating condition with a relatively calm and controlled flow and turbine behaviour. With these repetition points, the stability of the system and sensors can be monitored through out the experiment, and temperature drift could be compensated for.

Temperature compensation

The attempted temperature compensation performed during post-processing after the first experiment is explained in detail in Paper 3 [28].

For the second iteration of the experimental setup, manual adjustment of the trimmer potentiometers were required regularly. The procedure used was that after a finished measurement series, or after the rig temperature equalising to the water at the beginning of a day, the rig would be stopped while still submerged. The potentiometer of R_2 was tuned until the bridge output was as close to 0V as possible for all five bridges. Then the rig would be restarted and set to the repetition point. Some time would be given to allow for the temperatures to fully equalise again before taking the repetition point. After going through the measurement points of interest for that series, a final repetition point was taken before stopping the rig and repeating the adjustment. With these two repetition points at the beginning and end of a series, it was hoped that a *reference strain* could be used to offset the measured strain through each series and some sort of relative mean strain values could be extracted from the data as well. This has however not been done yet.

Post-processing

All of the recorded data in LabVIEW was saved as *.TDMS* files, a structured binary file format by National Instruments. The data in these files were extracted, converted, organised, analysed and visualised in MATLAB. To extract the peak to peak strain values presented in Paper 4 [36] were calculated by first *detrending* the data to avoid slopes in the mean over time to affect the total reported peak to peak and only considering 97% of the values around the mean to remove spurious spikes. The presented FFT data in this thesis were calculated through Welch's windowing method. For the contour plots presented in both Paper 3 and 4, interpolation between each measured point was used, which is also described in Paper 4.

Chapter IV

Summary of papers

■ This chapter contains a brief summary of the papers included in Part II. The summary also attempts to show the different phases of this PhD, some of the methods developed, challenges encountered and the final results of the experiments.

Paper 1 - High flexibility in Francis turbine operation and design philosophy: A review

J.O. Kverno, I. Iliev, & O.G. Dahlhaug. Published in IOP Conf. Series: Earth and Environmental Science, 2022

Authors contribution statement: J.K.: Conceptualisation, writing original draft and editing. I.I.: Supervision, review and evaluation. O.G.D.: Review and editing, supervision.

As a starting point for this PhD project, this paper aims to investigate and analyse various operation schemes and design philosophies to extend the expected lifetime of a hydro turbine exposed to numerous start-stop cycles and high ramping rates. The growing adoption of renewable and non-dispatchable energy sources in Europe has increased the demand for flexible operation within the rest of the power system. The Norwegian power system is in a unique position given its large number of hydropower plants with a rapid response capability, and thus holds significant potential to act as a stabiliser for mainland Europe. However, the shift towards more flexible operation can subject the turbines to higher load variations, potentially leading to premature fatigue and turbine failure. This study evaluates the current startup and ramping schemes, as well as touching upon some design aspects that may influence or mitigate the mechanical stresses experienced by the hydro turbine.

Paper 2 - Calibration of strain gauges on a model runner blade combining numerical and experimental data

J.O. Kverno, I. Iliev, B.W. Solemslie & O.G. Dahlhaug. Reviewed and accepted for publication in IOP Conf. Series: Journal of Physics, Q4 2023

Authors contribution statement: J.K.: Conceptualisation, writing original draft and editing, data gathering, software and analysis. I.I.: Conceptualisation of calibration rig and numerical setup and analysis, review and evaluation. B.W.S.: Supervision, post processing and analysis, review and editing. O.G.D.: Review and editing, supervision.

This paper presents the methodology, setup, and results of calibrating a set of strain gauges fixed to the trailing edge of the runner blades of a model Francis turbine. The calibration process is an essential step within the HydroFlex project, aiming to acquire experimental data to validate numerical models and enhance the estimation of the turbine's reduced lifetime resulting from increased flexibility in its operation. Due to the intricate geometry of the blade, obtaining an analytical solution for stresses under specific loads is unfeasible, necessitating the calibration procedure. To achieve this, a combination of strain measurement and numerical analysis is utilised to establish a direct correlation between the strain gauges' response and the strains parallel to the trailing edge. The strain gauges are installed on the suction side of the blades, near the hub and shroud, and the calibration is conducted by applying known weights to the shroud using a custom-made blade fixture. The signals from the sensors are processed through a set of miniature amplifiers, which conveniently fit within the hub of the model runner. The numerical simulation is implemented in ANSYS Mechanical, designed to fully replicate the physical setup's conditions. The results demonstrate the viability of the calibration method, albeit revealing a challenge related to the response, requiring additional amplification due to the stiffness of the runner blade material.

Paper 3 - Challenges with onboard strain measurements on a model Francis turbine runner

J.O. Kverno, G.E. Vefring, I. Iliev, B.W. Solemslie & O.G. Dahlhaug. Reviewed and accepted for publication in IOP Conf. Series: Journal of Physics, Q4 2023

Authors contribution statement: J.K.: Conceptualisation, writing original draft and editing, data gathering, software and analysis. G.E.V: Measurement setup and data gathering, post processing and analysis. I.I.: Post processing and analysis,

supervision, review and evaluation. B.W.S.: Supervision, post processing and analysis, review and editing. O.G.D.: Review and editing, supervision.

In this paper an experimental setup and the results obtained from a measurement campaign conducted on a model of a low specific speed Francis runner is presented. The measurements were taken using strain gauges mounted at the trailing edge of two runner blades. A significant amount of electrical noise in the strain measurement compounded with the low response of the gauges, which lead to no viable measurements of the vibrations of the blade. The mean of the measured strain was also investigated. The results reveal a significant drift in the mean strain over time during the measurement campaign and a lower measured strain at BEP (Best Efficiency Point) than anticipated when compared to numerical simulations. Through this paper, the experimental setup is presented. The obtained results are also presented, and the encountered challenges discussed.

Paper 4 - Onboard measurements with strain gauges on a model Francis runner

J.O. Kverno, I. Iliev, B.W. Solemslie & O.G. Dahlhaug. Submitted to: Energies

Authors contribution statement: J.K.: Conceptualisation, writing original draft and editing, data gathering, software and analysis. I.I.: Conceptualisation of model runner design, analysis, supervision, review and evaluation. B.W.S.: Supervision, analysis, review and editing. O.G.D.: Review and editing, supervision.

This paper focuses on presenting the experimental setup and outcomes from a revised measurement campaign conducted on a model of a low specific speed Francis runner. This research builds upon and refines the authors' previous work, as mentioned in the summary of Paper 3. More sensitive strain gauges were used to measure strain at the trailing edge of two runner blades. Comprehensive measurements were performed over a wide range of speed- (n_{ED}) and discharge factors (Q_{ED}), enabling an analysis of how dynamic strain at the trailing edge is influenced by these parameters. This paper presents an overview of the experimental setup along with the improvements made to it. Additionally, some of the obtained results are presented and discussed, shedding light on the impact of flexible operation on the mechanical behaviour of Francis turbines. Finally, it shows that it is fully possible to do strain gauge measurements on the model turbine scale, and that the general trends typically seen in prototypes are also seen here.

Chapter V

Results and Discussion

■ This chapter will present and compare some of the results from the two measurement campaigns and try to support the validity of the data.

The rest of this page is intentionally left blank so both the text and relevant figures are visible to the reader in each section.

5.1 Strain gauge signals

In figure 5.1 a comparison of the measured strain near the hub during the two experimental campaigns at the same operating conditions, but with different strain gauges is presented. Both signals have been shifted to the zero axis for this comparison. While the signal from the second campaign can be seen to have a cyclic oscillation, albeit small with this scaling, the signal from the first campaign is hard to decipher due to the noise.
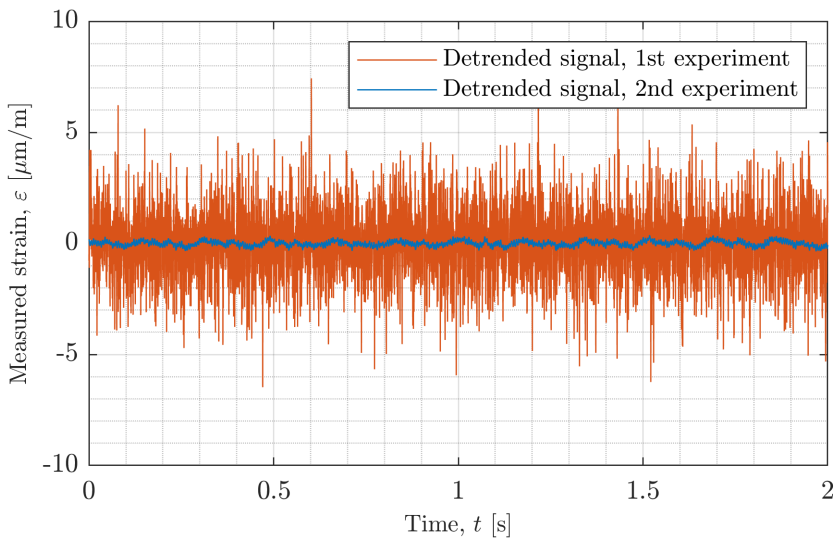
Figure 5.1: Comparison of the measured strain during the two experimental campaigns, both from BEP at 13m head.

5.2 Peak to peak

Figures 5.2 and 5.3 are both showing the measured peak to peak strain at various operating conditions. Most points were taken at 12m head, except for *Peak stress*, which was taken at 30m. Note that $Ss2$ had a more severe drift away from zero during the the first campaign compared to the other three strain gauges, causing the signal to clip by the time the final two points were taken.
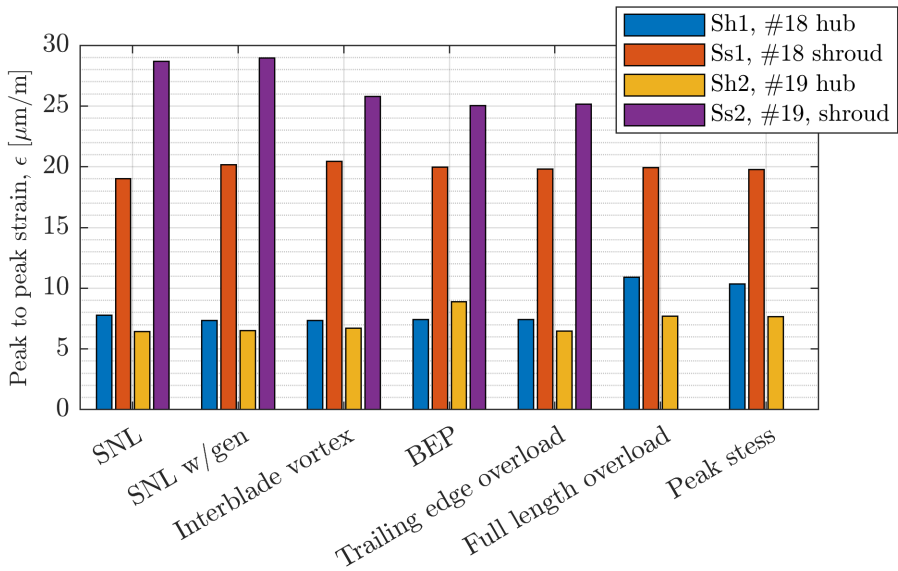
Figure 5.2: Peak to peak strain at various operating conditions during the first experimental campaign.
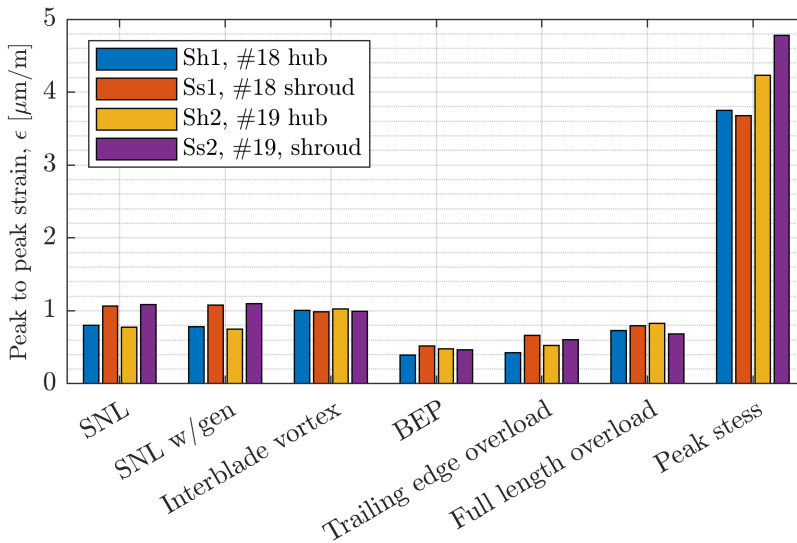
Figure 5.3: Peak to peak strain at various operating conditions during the second experimental campaign.

5.3   FFT and validation

The figures 5.4 and 5.5 shows the most dominating frequencies in the recorded strain while the turbine was operating at a constant speed factor of 0,18 and with an increasing guide vane opening. While mostly sharing the dominating frequencies, some differences do appear. In both figures, one peak at 28 times the rotational frequency is clearly defined. The source of this peak is the blade passing frequency of the guide vanes, as the turbine test rig has 28 of them. Although not too clear from the grayscale, the peak at 28 times f_n is higher near the hub than at the shroud. Another constant peak through all the measurements is the rotational frequency itself, and near the shroud it is the most dominating one. At the hub however, the RVR has the highest peak in the FFT, and it has a frequency of $\approx 0,63 \cdot f_n$. The final more prominent frequency is $2 \cdot f_n$, and it is believed to be a harmonic of f_n. Note that the results presented here are in the base 10 logarithm of the amplitude, since the absolute amplitudes of Rheingans at the hub, and the rotational frequency at the shroud were orders of magnitude larger than most other peaks in the FFT. The x-axis has been limited to 36 times the rotational frequency, simply because there was nothing of importance to be seen higher up.
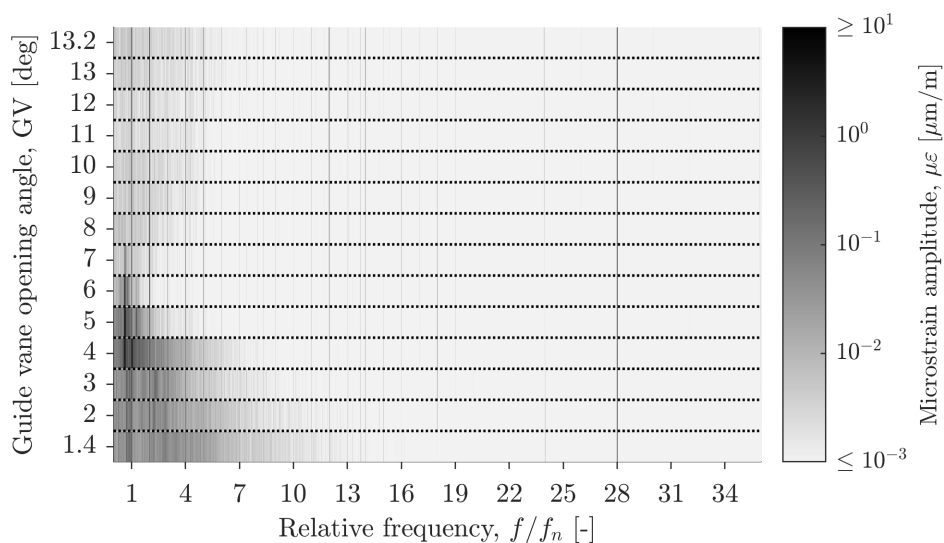
Figure 5.4: Results from the FFT analysis of the measured strain near the hub during *synchronous speed operation* at 20m head.
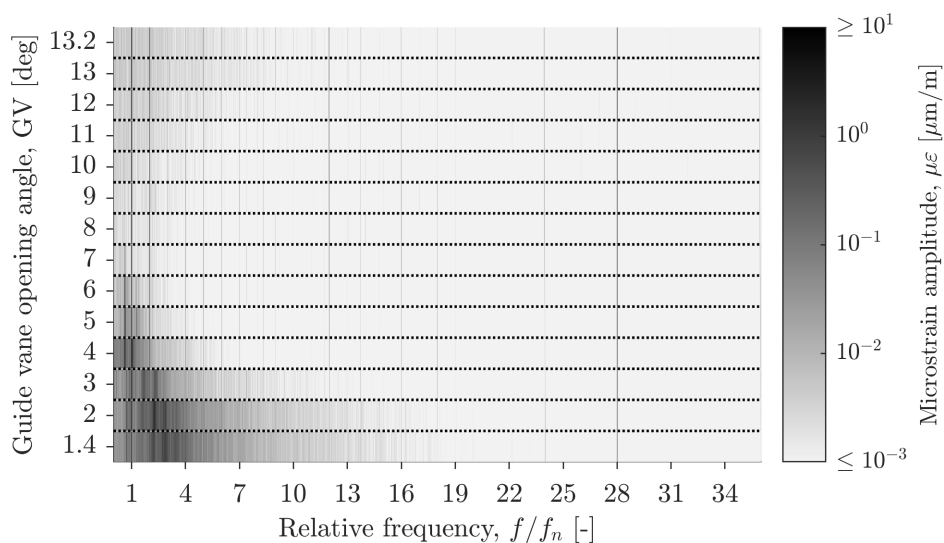
Figure 5.5: Results from the FFT analysis of the measured strain near the shroud during *synchronous speed operation* at 20m head.

5.4   Repeatability in the measurements

Another measure of the quality of experimental results are repeating behaviours and trends. Figure 5.6 shows the measured peak to peak strain at the repetition measurement performed throughout the second campaign, showing very little deviation for each strain gauge. Figure 5.7 shows the measured peak to peak strain for various operation points following a speed factor of 0,18, i.e. closely resembling synchronous speed operation. These measurements were done twice, and the first set (*init*) was done at the very beginning of the experiment in question, and the second set (*rep*) was repeated at the very end several days later. Apart from some deviation at deep part load, and the $Sh1$ strain gauge perhaps needing calibration to due to an apparent issue with the response, they all seem to follow each other nicely. Even with the slope of $Sh1$ not following the other three, and especially $Sh2$, the trend is again consistent and it repeats itself. The sudden jump in peak to peak strain near the hub at 4°opening angle seems to come from the RVR in the draft tube as also seen in the FFT analysis, and this is naturally more prominent near the hub than the shroud at such low discharges.
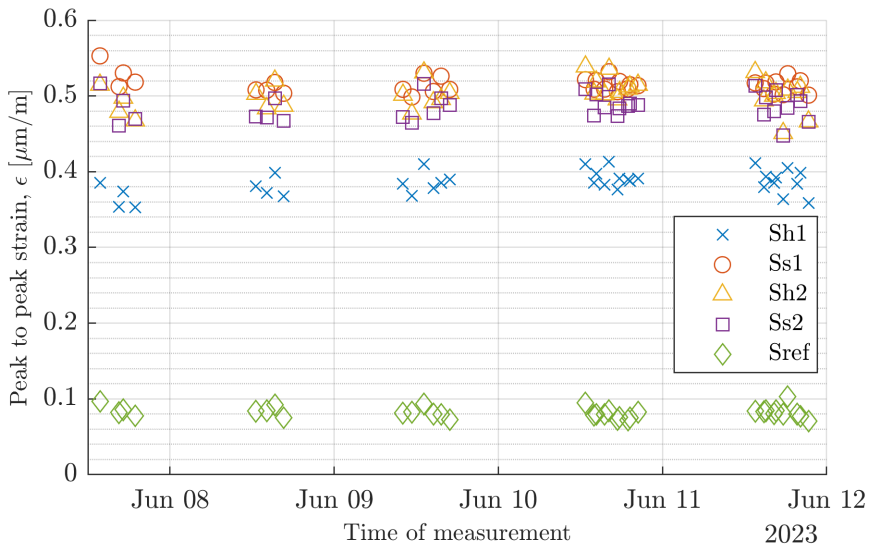
Figure 5.6: Measured peak to peak strain at the repetition points throughout the second measurement campaign.
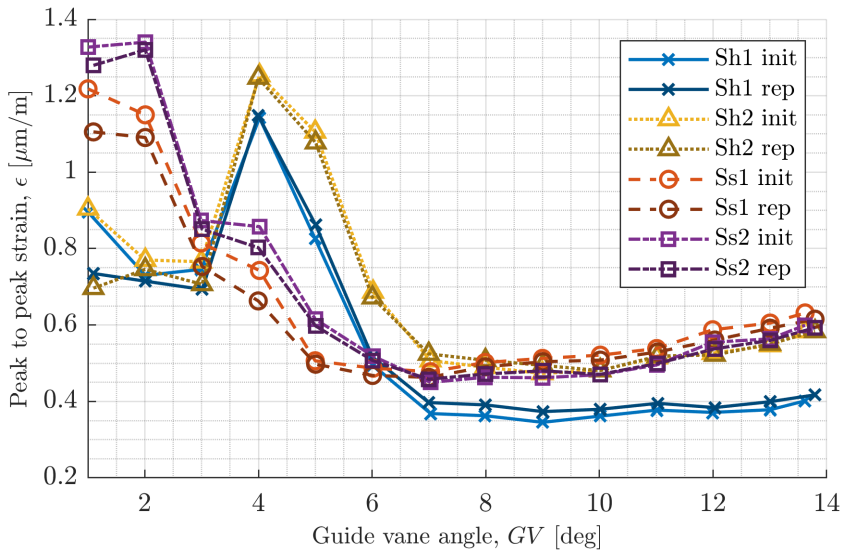
Figure 5.7: Measured peak to peak strain at the very beginning and very end of the second measurement campaign.

Chapter VI

Conclusions and Further work

◼ In this chapter, some final conclusions and suggestions for further work, both with the data at hand in the short term, and some more general ideas for the long term.

6.1   Conclusions

To meet the new demands put on the grid and energy producers with the proliferation of non-dispatchable and intermittent sources, an increased demand for flexibility is to be expected from other energy sources on the grid, such as hydropower turbines. In order to meet this new demand, dispatchable sources have to adjust their energy output accordingly since the energy produced at any time must be consumed. With hydropower being one of the most flexible energy sources, it is in an excellent position to meet these new operation schemes. Extended operation at off-design conditions, more frequent start-stops and ramping will undoubtedly increase the fatigue loading and shorten the lifetime of the unit. Therefore the natural development moving forward is to better quantify the cost of flexible operation and predict when inspections are needed, of which this study can lay a good foundation for.

The data gathered for this thesis proves both the viability of strain gauge measurements on low specific speed model turbines of this scale and that similar behaviours and trends typically seen on prototype scale measurements are also seen on the model scale. While a proper calibration of more sensitive strain gauges with controlled temperature has yet to be performed, it is believed that using the method presented in Paper 2, strain can be measured also as a mean or absolute value offset from a known baseline. Finally, a new runner design and relatively vast amount of onboard strain gauge measurement data from the runner is opened up to the

public, increasing our understanding of the cost of flexible operation and enabling the creation of new models and tools to estimate lifetime reduction.

6.2   Further work

Due to the amount of data gathered, far from all of it has been thoroughly processed and analysed, so the first and probably lowest hanging fruit in terms of further work is just that. If the repetition points taken are good and consistent, they could be used as a baseline for quantifying the mean strain at the trailing edge of the blades. Secondly, a proper calibration of the second set of blade mounted strain gauges with temperature control should be done, both to confirm their consistency in the response from cyclic loading at various temperatures within the expected range, and to quantify the uncertainties in the already performed measurements.

More broadly speaking, the measurements and methods applied should be repeated on different designs and mid/higher specific speed turbines for validation. Using the measurements, the setup, and procedures developed as a starting point more measurements of the same type should be done, on both other runner designs and specific speeds, compared to the F-101. These new measurements can be added to create generalised models and tools for lifetime estimation based on operation conditions. Then, the basis for a more generalised model for the lifetime estimation based on operation patterns can be built.

References

[1] Copernicus Programme - European Commision. *July 2023: Global air and ocean temperatures reach new record highs*. Press release. Aug. 2023.

[2] European Commission. *A policy framework for climate and energy in the period from 2020 to 2030.* 2014.

[3] European Commission. *A clean planet for all. A European strategic long-term vision for a prosperous, modern, competitive and climate neutral economy*. 2018.

[4] Stefan Weitemeyer et al. 'Integration of Renewable Energy Sources in future power systems: The role of storage'. In: *Renewable Energy* 75 (2015), pp. 14–20. ISSN: 0960-1481.

[5] Seming Skau et al. *Kraftproduksjon*. 2023. URL: `https://nve.no/energi/energisystem/kraftproduksjon/` (visited on 10/08/2023).

[6] *Kulturminner i norsk kraftproduksjon : en evaluering av bevaringsverdige kraftverk (KINK)*. nob. Rev. utg. Vol. nr. 52 - 2013. Rapport (Norges vassdrags- og energidirektorat : online). Oslo: Norges vassdrags- og energidirektorat, 2013. ISBN: 9788241009211.

[7] Norwegian University of Science and Technology. *HydroFlex - Increasing the value of Hydropower through increased Flexibility*. URL: `https://www.h2020hydroflex.eu/` (visited on 20/01/2023).

[8] Einar Kobro. 'Measurement of pressure pulsations in Francis turbines'. eng. PhD thesis. Trondheim, 2010. ISBN: 9788247122396.

[9] Katarina Kloster. *Trykkpulsasjoner inne i et Francis løpehjul*. nor. 2016.

[10]   Mohamed Farhat et al. *Onboard Measurements of Pressure and Strain Fluc-tuations in a Model of low Head Francis Turbine. Part 1 : Instrumentation*. eng. 2002.

[11]   Pierre Yves Lowys et al. *Onboard Measurements of Pressure and Strain Fluctuations in a Model of low Head Francis Turbine. Part 2 : Measurements and Preliminary Analysis Results*. eng. 2002.

[12]   U. Seidel et al. 'Dynamic loads in Francis runners and their impact on fatigue life'. In: *IOP Conf. Series: Earth and Environmental Science*. 2014.

[13]   Dietmar Gross. *Mechanics of Materials – Formulas and Problems : Engineering Mechanics 2*. eng. Berlin, Heidelberg, 2017.

[14]   R. Viswanathan and R. Tilley. '23 - Creep damage – industry needs and future research and development'. In: *Creep-Resistant Steels*. Ed. by Fujio Abe, Torsten-Ulf Kern and R. Viswanathan. Woodhead Publishing Series in Metals and Surface Engineering. Woodhead Publishing, 2008, pp. 637–666. ISBN: 978-1-84569-178-3.

[15]   Anthony J Wheeler. *Introduction to engineering experimentation*. eng. Boston, 2010.

[16]   D Frunzăverde et al. 'Failure analysis of a Francis turbine runner'. In: *IOP Conference Series: Earth and Environmental Science* 12.1 (Aug. 2010), p. 012115.

[17]   A. Lyutov et al. 'Modelling of a Francis Turbine Runner Fatigue Failure Process Caused by Fluid-Structure Interaction'. In: *IOP Conference Series: Earth and Environmental Science* 49.7 (Nov. 2016), p. 072012.

[18]   Einar Agnalt. 'Rotor-Stator Interaction in Low-Specific Speed Francis Turbines'. eng. PhD thesis. 2019. ISBN: 978-82-326-4035-5.

[19]   Peter Dörfler, André Coutu and Mirjam Sick. *Flow-Induced Pulsation and Vibration in Hydroelectric Machinery: Engineer's Guidebook for Planning, Design and Troubleshooting*. eng. 1. Aufl. Springer Verlag London Limited, 2013. ISBN: 9781447142515.

[20]   Joachim Raabe. 'Hydro power. The design, use, and function of hydromechanical, hydraulic and electrical equipment'. In: (1985).

[21]   Thomas Neidhardt, Marcelo Magnoli and John Gummer. 'High part-load fluctuations in Francis turbines and the applicability of model test data'. In: *Hydro 2017* (2017).

[22]   W. J. Rheingans. 'Power Swings in Hydroelectric Power Plants'. In: *Transactions of the American Society of Mechanical Engineers* 62.3 (Feb. 2023), pp. 171–177. ISSN: 0097-6822. eprint: `https://asmedigitalcollection.asme.org/fluidsengineering/article-pdf/62/3/171/6988607/171\_1.pdf`.

[23]   Hermod Brekke. *Pumper og turbiner : kompendium*. nob. Trondheim, 2003.

[24]   Halvard Bjørndal, Trond Moltubakk and Hans Aunemo. 'Flow induced stresses in a medium head Francis runner – Strain gauge measurements in an operating plant and comparison with Finite Element Analysis'. In: June 2001.

[25]   Eduard Doujak and Markus Eichhorn. 'An Approach to Evaluate the Lifetime of a High Head Francis Runner'. In: 2016.

[26]   Julian Unterluggauer, Eduard Doujak and Christian Bauer. 'Fatigue analysis of a prototype Francis turbine based on strain gauge measurements'. In: *WASSERWIRTSCHAFT* 109 (Sept. 2019), pp. 66–71.

[27]   Johannes Kverno et al. 'Calibration of strain gauges on a model turbine blade combining numerical and experimental data'. In: *Journal of Physics: Conference Series* (2023).

[28]   Johannes Kverno et al. 'Challenges with onboard strain measurements on a model Francis turbine runner'. In: *Journal of Physics: Conference Series* (2023).

[29]   International Electrotechnical Commission. *60193:2019 Hydraulic turbines, storage pumps and pump-turbines - Model acceptance tests.* 2019.

[30]   Ole Gunnar Dahlhaug et al. *Tokke model test 2006-2007*. Tech. rep. Waterpower Laboratory, Institute for Energy and Process Engineering, NTNU, June 2007.

[31]   Einar Kobro, Torbjørn Kristian Nielsen and Ole Gunnar Dahlhaug. 'Data analysis from onboard francis model runner pressure measurements'. In: *13th International Symposium on Transport Phenomena and Dynamics of Rotating Machinery 2010, ISROMAC-13*. 2010, pp. 98–103.

[32]   Norwegian Hydropower Centre. *Francis-99*. URL: `https://www.ntnu.edu/nvks/francis-99` (visited on 20/01/2023).

[33] Igor Iliev et al. 'Optimization of Francis Turbines for Variable Speed Opera-
      tion Using Surrogate Modeling Approach'. 101214. PhD thesis. Aug. 2020.
      eprint: `https://asmedigitalcollection.asme.org/fluidsengi
      neering/article-pdf/142/10/101214/6554501/fe_142_10
      _101214.pdf`.

[34] Norwegian University of Science and Technology. *HydroCen*. URL: `https:
      //www.ntnu.no/hydrocen` (visited on 20/01/2023).

[35] Igor Iliev. *HydroFlex D3.4 - Hydraulic and mechanical design of the Francis
      model turbine*. Tech. rep. 2020.

[36] Johannes Kverno et al. 'Onboard measurements with strain gauges on a
      model Francis runner'. In: (2023).

[37] Hottinger Baldwin Messtechnik GmbH. *Strain Gauges - Absolute precision
      from HBM*. 2018. URL: `https://pdf.directindustry.com/pdf/hb
      m-test-measurement/hbm-estrain-gauge-catalog/6017-2667
      31.html#open614644` (visited on 20/01/2023).

[38] Inc. Kulite Semiconductor Products. *Kulite Strain gage series*. URL: `https:
      //kulite.com/assets/media/2017/06/Strain-Gage-Series.p
      df` (visited on 20/01/2023).

[39] Mantracourt. *ICA emedded strain gauge analogue amplifiers*. 2018. URL:
      `https://www.mantracourt.com/userfiles/documents/ica_us
      er_manual.pdf` (visited on 26/01/2023).

[40] Vishay Foil Resistors, VPG. *High precision foil resistor with TCR of
      $\pm2.0ppm/^\circ C$, tolerance of $\pm0.005\%$ and load life stability of $\pm0.005\%$.*
      2015. URL: `https://foilresistors.com/docs/63001/63001.pdf`
      (visited on 26/01/2023).

Part II

Papers

Paper 1

High flexibility in Francis turbine operation and design philosophy: A review
Kverno, J. O., Iliev, I. and Dahlhaug, O. G.
IOP Conference Series: Earth and Environmental Science vol. 1037 012011, 2022

High flexibility in Francis turbine operation and design philosophy: A review

J O Kverno[1*], I Iliev[2] and O G Dahlhaug[1]

[1] Department of Energy and Process Engineering, Norwegian University of Science and Technology, Alfred Getz' vei 4, 7034 Trondheim, Norway
[2] SINTEF Energi AS, Sem Sælands vei 11, 7034 Trondheim, Norway

[*] E-mail: `johannes.kverno@ntnu.no`

Abstract. This paper examines and discusses how various operation schemes and design philosophies can prolong the expected lifetime of a hydro turbine subjected to many start-stop cycles and high ramping rates. With the proliferation of renewable and non-dispatchable energy sources in Europe, a higher demand for flexible operation is put on the rest of the system. Given the short response time of hydro power, there is a huge potential for the Norwegian power sector to act as a stabiliser for the rest of mainland Europe. With a more flexible operation however, the turbines will experience a higher load variation which can lead to premature fatigue and failure of existing turbines. This research reviews the current startup and ramping schemes, as well as design aspects, which might affect and reduce the mechanical stresses experienced by the hydro turbine.

Keywords: Fatigue loading, Flexibility, Francis turbine

1. Introduction and Background

The 2030 climate & energy framework of the European Union states that by 2030, CO_2 emissions should be reduced by 40% from the 1990 levels, and at least 32% of the energy production shall come from renewable sources [1].

With the increased use of wind turbines and photovoltaic panels, which are so called non-dispatchable energy sources, the demand for more flexible and varied operation of traditional energy production is needed in order to maintain a stable frequency on the power grid [2]. According to Weitemeyer et al [3], up to about 20% of the energy demand can be met by intermittent energy sources without any major issues with grid stability, meaning; to reach the 2030 goal, both in terms of an increased use of renewables and a cut in CO_2

emissions, hydro power is the perfect source fill in the gap as already seen in the Nordic grid [4]. Hydro power is one of the more flexible sources of energy and can typically go from a cold start-up to full load within a few minutes [5]. Additionally, hydro turbines can rapidly change the power output depending on the requirements and thus can be operated in a fashion which helps to counteract the changes in the grid frequency and voltage, which is directly linked to the mismatch between the supply and demand of energy in the grid. This operation scheme does put an increased mechanical load on existing hydro turbines, as they traditionally were designed and constructed to operate in a more predictable and stable manner [6]. This can ultimately lead to premature fatigue damages and costly downtime [7]. In this paper, the existing research on increased fatigue loads due to flexible operation of Francis turbines will be reviewed. The work behind this paper is a part of a larger project, HydroFlex, a multidisciplinary research project working towards increasing the flexibility of hydro power while also mitigating the environmental impacts.

2. Flexibility and turbine fatigue

During a start-stop cycle a Francis turbine will experience fatigue loads due to pressure oscillations, leading to cyclic loads with high stress amplitudes. This was illustrated when a Francis runner cracked after only 1067 working hours, and 422 startups [8, 9]. After the incident, a methodology developed to estimate the runner fatigue lifetime showed that the cracking could not have happened unless the turbine was operated with many start-stop cycles. Another power plant, with five identical high specific speed units developed visible cracking on three of the units after a mere 700 to 1500 hours of operation in a load peaking manner, leading to several start/stop cycles per day [10]. However, it has been demonstrated [11] that just by altering the guide vane opening scheme during a startup procedure, the overall cyclic loading on the runner can be drastically reduced due to a lower amount of high frequency pressure oscillation in the flow. This show that the expected lifespan of the runner can be extended, compared to a unit started using a non optimised startup scheme. Another thing to consider is the load variation during operation, and how much it will affect the runner [12, 13]. Introducing variable speed operation can reduce pressure pulsations in the turbine, thus reducing the fatigue loads [14, 15, 16]. During operation of traditional Francis turbines, there are several types of flow disturbances and oscillations which causes mechanical stress and fatigue on the unit. Traditional turbines are designed to operate at a narrow range close to the design point [6], and moving away from this best efficiency point (BEP) introduces different kinds of phenomena, depending on the load. During startup, the angle of the incoming flow and the angle of the leading edge of the runner blade will have a large mismatch, leading to flow separation and the generation of vortices travelling down the blade channels, leading to stress on the runner blades. These interblade vortices are typical

for low part loads as well ($<$ BEP). At part load, a rotational component of the flow appears in the draft tube while the total volumetric flow rate is low, causing a vortex breakdown and reversed flow in the centre of the draft tube. Above $\sim 50\%$ of BEP, and if the pressure in the draft tube is low enough, cavitation might appear in a helix shaped vortex, and this vortex will rotate around the zone of reversed flow in the centre with a rotational frequency of $f_R \approx \frac{1}{3} f_n$. Due to the low pressure of this vortex rope there will be a rotating pressure field in the cross section of the draft tube, and at the elbow of the draft tube this asymmetrical pressure field might lead to a plunging flow, leading to cyclic mechanical loading on the turbine [17]. When operating at full load ($>$ BEP), there will also be a rotational component in the draft tube, albeit in the opposite direction of the turbine rotation. The volumetric flow is also high, meaning that a cavitated vortex in the centre of the draft tube will remain axisymmetric, as seen in figure 1.
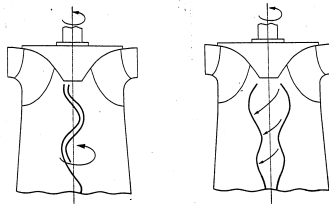
Figure 1: Part-load and full load vortices in the draft tube [18].

Francis turbines will also experience a phenomena called rotor-stator interaction (RSI). The cause of this is the throttling effect a runner blade has as it passes in front of the flow exiting the guide vane channels, leading to a higher pressure as the velocities drop [19]. The end result is that a rotating pressure field appears in the vaneless space with a frequency as a function of the rotational velocity and the number of runner blades (stationary frame of reference) or guide vanes (rotating frame of reference). If the frequency of the RSI or a harmonic of this frequency coincide with the resonant frequency of the turbine, fatigue damage can appear, in the matter of hours even in some cases [20]. If variable speed operation is introduced the frequency of the RSI is no longer fixed but rather move with the rotational speed, meaning that extra care needs to be taken to avoid getting in to resonance at certain operating conditions or speeds of rotation, and the resonant frequencies of the unit in question might have to be mapped out during commissioning so a complete and safe range of operation schemes can be made.

3. Current research
The end goal of the PhD work behind this paper is to perform model tests on a Francis turbine to validate numerical simulations of startup conditions.

One key to reducing the fatigue load during a startup sequence, is to optimise the procedure with this in mind. Gagnon et al. [11] did an investigation on how the startup scheme affects the expected lifetime of a Francis runner. They combined theoretical models to estimate crack growth with experimental data from strain gauge measurements on a prototype runner at Beauharnois power plant to get a better understanding of how two different startup schemes alter the runners expected lifetime, as seen in figure 2. The main variable that was changed during startup was the opening degree of the guide vanes. The results showed that just by reducing the opening from 40-50% to just above 30%, the crack growth rate was drastically reduced.

(a) Startup scheme 1   (b) Startup scheme 2
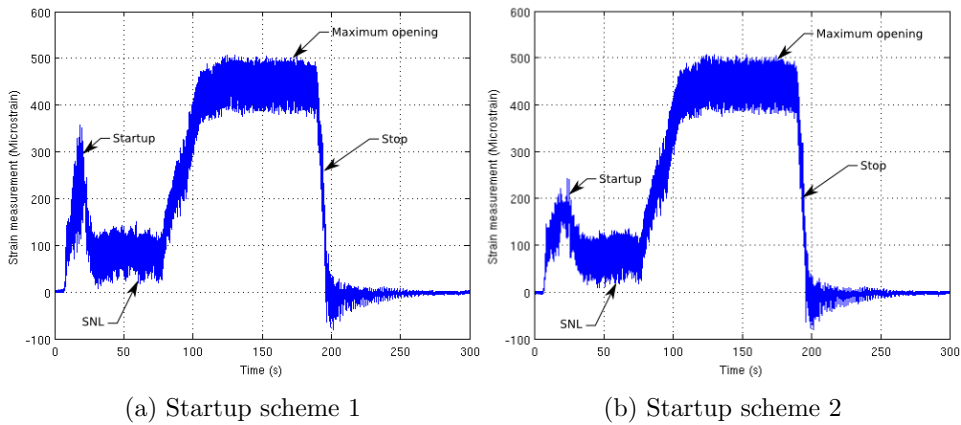
Figure 2: Comparison of strain measurements between the two types of startup schemes showing the reduced strain experienced during startup with the more gentle startup scheme, Gagnon et al. fig. 6 [11].

Another factor which plays in to the fatigue damages to a turbine is how the unit is operated. A turbine providing base load to the grid will tend to operate close to the BEP and in general have few start-stop cycles and thus little to no reduction to the expected lifespan. However, a unit operated for grid stabilisation tends to have more frequent startups, and more operation time spent further from the BEP, as Seidel et al [22] demonstrated. Through experimental measurements on an operating prototype turbine, model turbine experiments and advanced numerical simulations a better understanding of the different factors which inflict damage to Francis turbines was gained. The results showed that a turbine operating in a base load scenario experiences less than 15% of the relative damage, compared to a grid stabilisation unit (figure 3). The main contributors to the damage was the startup, speed no load (SNL) and low part load. One key finding was that to operate the turbines more flexibly the operation sequences should be optimised, which has not typically been done before.
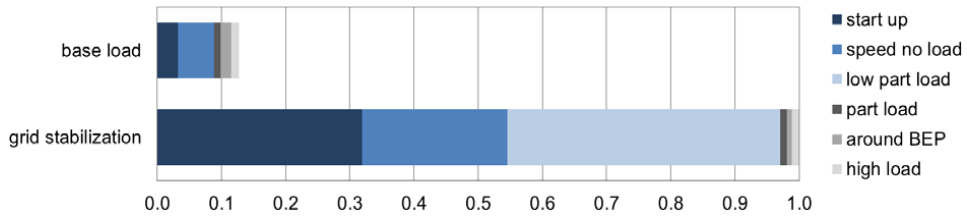
Figure 3: Comparison of the relative damage inflicted by the two operating schemes, Seidel et al. fig. 1 [22].

Halvar Bjørndal et al [21] demonstrated however that the rated head, or specific speed, of a turbine also plays a role when evaluating the main causes of fatigue. Several different Norwegian hydro power plants had been investigated, and it was found that while higher specific speed machines were mostly experiencing failures and blade cracking due to SNL and low part load conditions, meaning that higher part loads and up to full load (above BEP) were unproblematic. Low specific speed turbines however were more susceptible to other phenomena which causes cyclic loading as well, namely RSI. The measured RSI induced blade stress frequencies were also higher than the ones observed from startup and SNL on high specific speed units. The author also concludes that the operator/plant owner should be more specific about how the turbine is to be operated when they put out a tender.

Chirag Trivedi et al. performed a series of pressure pulsation measurements on a model Francis runner [23] and two different prototypes [24]. The main focus of the model experiment was to investigate the flow behaviour during SNL conditions utilising pressure transducers in both the stationary and rotating domain. Both transient and steady state conditions were investigated with the latter at the design speed of the turbine. The results showed an increasing pressure pulsation amplitude in the vaneless space as the wicket gate opened, and at SNL the amplitudes were nearly twice that which occurs during normal operation. An increase in pressure and strain has also been demonstrated numerically on different turbine designs [25, 26]. On the two prototypes pressure was only measured from the draft tube walls, close to the runner outlet [24]. The prototypes were of similar specific speed but different orientation, one vertical- and one horizontal axis turbine. The authors found that both during the initial phase of wicket gate opening and during generator synchronisation the pressure pulsations reached amplitudes of 3,5% of the head, or 2,8 times greater than at BEP. The pulsations were stochastic in nature, i.e. no sign of a vortex rope, and remained even after synchronisation. There were also considerable pulsations during transients with amplitudes of up to 1,6 times that of steady state operation, especially when operating further away from BEP. The orientation of the axis, and thus draft tube, also seemed to influence

the behaviour and the type of pressure pulsations. The dominating frequency in the measurements by Chirag Trivedi et al. seemed to be the RSI, and the same can be seen in measurements performed at EPFL in 2004 on a low specific speed model Francis turbine and the associated numerical simulations done by Mélissa Fortin et al. [27].

Resonance in a turbine can cause a failure in a matter of hours, but accurately predicting the effects of pulsations and fatigue without empirical data from the turbine in question has previously not been done, leading to several cases of runners failing. However, as Petter Østby et al [28] demonstrated, important parameters such as the damping ratio can be calculated. With a more plausible damping ratio the numerical simulations of the fluid structure interaction becomes more accurate, and when the numerical simulations of three different high head Francis turbines were compared with experimental data of both on-board pressure and strain gauges, there were an agreement between the results. As expected the pressures had the smallest uncertainty and best agreement, while the dynamic stresses deviated a bit more. In Østby's case, the main focus was on the RSI, but it should still be applicable to other operating conditions as well.

4. Discussion

Flexible turbine operation implies a more frequent and/or rapid change in turbine operation, and since both far off-design conditions and transients have been shown to cause extra fatigue loading on turbines, a shorter lifetime or more frequent maintenance of existing units will probably be the end result [29]. Predicting the exact extent of fatigue damage on any particular unit given a set operation scheme is challenging, especially at deeper part loads due to the stochastic nature of the dynamic loading. Differences in fabrication and weld quality will also play a huge role in determining the mean time before failure (MTBF) [10]. Larger scale CFD simulations [30] and fluid-structure interaction (FSI) calculations [31] can be done to make more accurate predictions, but these are usually computationally demanding and not feasible in a commercial setting. Most Francis turbines are designed for a specific operating condition, and with a high efficiency as a relatively high priority. The best efficiency point (BEP) is typically at around 80% of full load, and as a consequence the conditions during start-up are further away from the optimum than what they would have been if the BEP was at a lower load. This can be better illustrated when looking at the velocity triangles at the inlet of the runner. As figure 4 illustrates, the mismatch between the relative flow angle and blade angle causes a flow separation and vortices on the suction side of the blade, as also seen in simulations [25]. These flow instabilities might then propagate through the blade channel towards the trailing edge of the blades, which is typically the location where premature fatigue and failure occurs [8, 10, 11, 20]. One
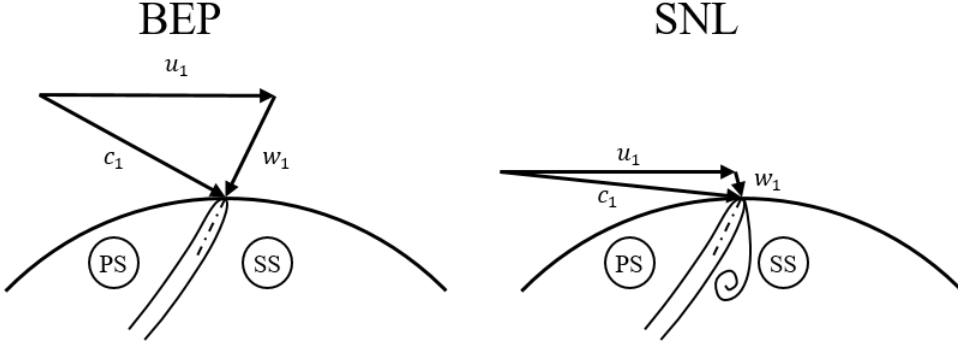
Figure 4: Inlet velocity triangles at BEP and SNL

possible solution to the problem of flow separation at the leading edge during SNL is to increase the angle of the runner blade to closer match the angle of the incoming flow. One drawback to this approach is that the BEP is moved to a higher head than what might have been originally intended. However, this might actually be beneficial for flexible operation, as the turbine might be better suited for a wider operating range with lower part loads. If variable speed operation is included as well the overall efficiency might be increased a bit, and the pressure pulsations reduced. Another possible solution to the problems of flow separation at SNL is to use an aerofoil profile more suited for higher angles of attack.

If we were to consider the Euler turbine equation and what happens at SNL, or runaway in general, the picture might not seem be the same as previously discussed.

$$g \cdot H_n \cdot \eta_h = u_1 \cdot c_{u1} - u_2 \cdot c_{u2} \tag{1}$$

With the naive assumption that the hydraulic efficiency at runaway is zero, or close to zero, the rotational component at the inlet of the turbine can be calculated from

$$c_{u1} = \frac{u_2 \cdot c_{u2}}{u_1} \tag{2}$$

For the example case of a high head Francis turbine, the rotational component is quite drastically reduced from the BEP, contradicting the first assumed behaviour. However, this would also mean that the energy leaving the runner at the outlet is equal to the energy entering at the inlet, which obviously isn't the case. In reality the energy at the inlet is the difference between the available energy from the head and the energy at the outlet of the runner, or

$$u_1 \cdot c_{u1} = g \cdot H_n - u_2 \cdot c_{u2} \tag{3}$$

Meaning that there is no simple way to get the velocity components at SNL. This is probably complicated with secondary flows and channel blockage not

being accounted for with the Euler equation as well. A more comprehensive model by Zhang [32] captures these effects better through the combination of the Euler turbine equation and the energy laws, and using some assumptions regarding the hydraulic efficiency and shaft torque. The model seems to make more accurate predictions regarding the speed ratio $\left(\frac{n_R}{n_N}\right)$, even compared to what is typically given by literature. By assuming a speed ratio of 1, which is the case at SNL, the GV angle and flow rate can be found, provided that the radial geometry of the blade is known.

5. Conclusion and further work

The main goal of the research in HydroFlex is to identify the locations most susceptible to fatigue damages during startup and high ramping, and this is to be done through a combination of numerical and experimental measurement campaign on a model Francis turbine at the Waterpower Laboratory at NTNU. A new model turbine is to be designed and manufactured through the HydroFlex project and its partners. The main goal of the measurement campaign on the model turbine is to acquire the required measurements and sensor installations on board the runner. The results from the experiment shall be used to validate numerical simulations of the fluid structure interactions. To get validation data for the CFD analysis a set of pressure sensors throughout the turbine and test rig can be used to gather data. Additionally, there is a possibility of getting PIV measurements in the vaneless space to get a better understanding of the flow field and velocities during the startup. For the validation of the material stress analysis (FEM), strain gauges will be utilised. To simplify the calibration of these sensors, the trailing edge of the runner blades will have a straight shape, as seen in figure 5. Additionally, to obtain a higher signal to noise ratio the runner blades will be made as thin as possible.
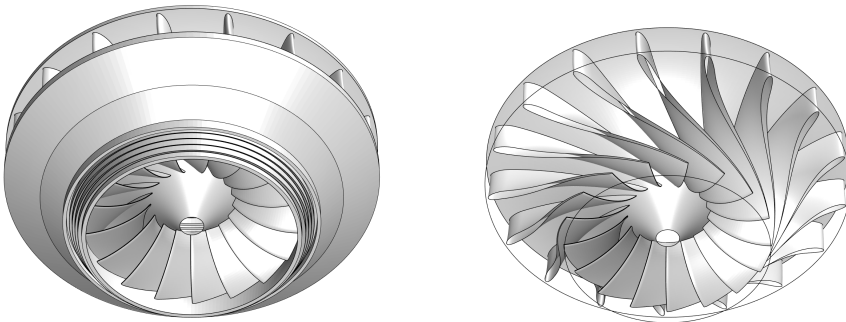

Figure 5: HydroFlex model runner design example with 17 runner blades and a straight trailing edge. The simple blade geometry can also be seen.

References
[1] European Commission 2014. A policy framework for climate and energy in the period
     from 2020 to 2030.
[2] Nardelli P H J, Rubido N, Wang C, Baptista M S, Pomalaza-Raez C, Cardieri P and
     Matti L 2014. Models for the modern power grid. *Eur. Phys. J. Spec. Top.* **223** 12
     2423–37 Oct 2014.
[3] Weitemeyer S, Kleinhans D, Vogt T and Agert C 2014. Integration of renewable energy
     sources in future power systems: The role of storage. *Renewable Energy* **75** 2015
[4] Huertas-Hernando D et al. 2017. Hydro power flexibility for power systems with variable
     renewable energy sources: an IEA Task 25 collaboration. *WIREs Energy Environ* **6** 1
     p220 2017
[5] Huggins R A 2010. *Energy Storage* 1st ed. (New York: Springer US) p. 60
[6] Song C C S and Chen X 1996. Simulation of flow through Francis turbine by LES method
     Proc. of the XVIII IAHR Symp. on Hydraulic Machinery and Cavitation 1 ed. E
     Cabrera, V Espert and F Martínez (Valencia: Poly technic University of Valencia)
     p. 267
[7] Yang W, Norrlund P, Saarinen L, Yang J, Guo W and Zeng W 2016. Wear and tear on
     hydro power turbines – Influence from primary frequency control *Renewable Energy* **87**
     1 88-95 2016.
[8] Lyutov A, Kryukov A, Cherny S, Chirkov D, Salienko A, Skorospelov V and Turuk P 2016.
     Modelling of a Francis turbine runner fatigue failure process caused by fluid-structure
     interaction *IOP Conf. Ser.: Earth Environ. Sci.* **49** 072012
[9] Flores M, Urquiza G and Rodríguez J M 2012. A fatigue analysis of a hydraulic Francis
     turbine runner *World Journal of Mechanics* **2** pp28-34 2012
[10] Gummer J H and Etter S 2008. Cracking of Francis runners during transient operation
     Hydropower & Dams, Issue Four **15** 2008
[11] Gagnon M, Tahan S A, Bocher P and Thibault D 2010. Impact of startup scheme on
     Francis runner life expectancy. *IOP Conf. Ser.: Earth Environ. Sci.* **12** 012107
[12] Farell C and Gulliver J 1987. Hydromechanics of variable speed turbines *Journal of
     energy engineering* **113** 1 pp. 1-13 1987
[13] Heckelsmueller G P 2015. Application of variable speed operation on Francis turbines
     Ingeniería e investigación **35** 1 pp. 12-16 2015
[14] Fraile-Ardanuy J, Wilhelmi J R, Fraile-Mora J J and Perez J I 2006. Variable-speed hydro
     generation: Operational aspects and control. *IEEE transactions on energy conversion*
     21 2 pp. 569-574 2006
[15] Iliev I, Trivedi C, Agnalt E and Dahlhaug O G 2019. Variable-speed operation and
     pressure pulsations in a Francis turbine and a pump-turbine. *IOP Conf. Ser.: Earth
     Environ. Sci.* **240** 072034
[16] Sannes D B, Iliev I, Agnalt E and Dahlhaug O G 2018. Pressure pulsation in a high
     head Francis turbine operating at variable speed. *J. Phys.: Conf. Ser.* **1042** 012005

[17] Wang Z and Lingjiu Z 2006. Simulations and Measurements of Pressure Oscillations Caused by Vortex Ropes. *Journal of fluids engineering* **128** 4 pp. 649-655 2006

[18] Brekke H 2014. Hydraulic Turbines *Design, Erection and Operation* (Trondheim: NTNU) Fig. 7.3 p. 92

[19] Agnalt E, Iliev I, Solemslie B W and Dahlhaug O G 2019. On the rotor stator interaction effects of low specific speed Francis turbines. *International J. of Rotating Machinery* **2019** 5375149

[20] Østby P T K 2019. *Dynamic Stress in High Head Francis Turbines* (Trondheim: Norwegian University of Science and Technology, Faculty of Engineering, Department of Mechanical and Industrial Engineering) pp. 3-5.

[21] Bjørndal H, Reynaud A P and Holo A L 2011. Mechanical robustness of Francis runners, requirements to reduce the risk of cracks in blades. *HYDRO 2011*, Prague

[22] Seidel U, Mende C, Hübner B, Weber W and Otto A 2014. Dynamic loads in Francis runners and their impact on fatigue life. *IOP Conf. Ser.: Earth Environ. Sci.* **22** 032054

[23] Trivedi C, Cervantes M J, Dahlhaug O G and Gandhi B K 2015. Experimental investigation of a high head Francis turbine during spin-no-load operation. *J. of Fluids Engineering - Transactions of the Asme, 137* (6), 061106/1-061106/10.

[24] Trivedi C, Gogstad P J and Dahlhaug O G 2017. Investigation of the unsteady pressure pulsations in the prototype Francis turbines during load variation and startup. *J. of Renewable and Sustainable Energy, 9* (6)

[25] Nicolle J, Morissette J F and Giroux A M 2012. Transient CFD simulation of a Francis turbine startup. *IOP Conf. Ser.: Earth Environ. Sci.* **15** 062014

[26] Nennemann B, Morissette J F, Chamberland-Lauzon J, Monette C, Braun O, Melot M, Coutu A, Nicolle J and Giroux A M 2014. Challenges in dynamic pressure and stress predictions at no-load operation in hydraulic turbines. *IOP Conf. Ser.: Earth Environ. Sci.* **22** 032055

[27] Fortin M, Nennemann B, Houde S and Deschênes C 2019 Numerical study of the flow dynamics at no-load operation for a high head Francis turbine at model scale *IOP Conf. Ser.: Earth Environ. Sci.* **240** 022023

[28] Østby P T K, Billdal J T, Sivertsen K, Haugen B and Dahlhaug O G 2016. Dynamic stresses in high head Francis turbines. *Hydropower & Dams, Issue Three*

[29] Gagnon M, Nicolle J, Morissette J-F and Lawrence M 2016. A look at Francis runner blades response during transients. *IOP Conf. Ser.: Earth Environ. Sci.* **49** 052005

[30] Mende C, Weber W and Seidel U 2016. Progress in load prediction for speed-no-load operation in Francis turbines. *IOP Conf. Ser.: Earth Environ. Sci.* **49** 062017

[31] Hübner B, Weber W and Seidel U 2016. The role of fluid-structure interaction for safety and life time prediction in hydraulic machinery. *IOP Conf. Ser.: Earth Environ. Sci.* **49** 072007

[32] Zhang Z 2017. Master equation and runaway speed of the Francis turbine. *J. of Hydrodynamics* 30(2):203-217

Paper 2

Calibration of strain gauges on a model runner blade combining numerical and experimental data
Kverno, J. O., Iliev, I., Solemslie, B. W. and Dahlhaug, O. G.

Calibration of strain gauges on a model runner blade combining numerical and experimental data

Johannes Kverno[1]*, Igor Iliev[2], Bjørn Winther Solemslie[3] and Ole Gunnar Dahlhaug[1]

[1] Department of Energy and Process Engineering, Norwegian University of Science and Technology, Alfred Getz' vei 4, 7034 Trondheim, Norway
[2] SINTEF Energi AS, Sem Sælands vei 11, 7034 Trondheim, Norway
[3] NINA, Høgskoleringen 9, 7034 Trondheim, Norway

* E-mail: `johannes.kverno@ntnu.no`

Abstract. In this paper, we present the calibration setup, method, and results for a set of strain gauges installed on the trailing edge of the runner blades of a model Francis turbine. The calibration work is done as a step in the HydroFlex project, with the goal of taking experimental data to validate numerical models to better estimate the reduction in lifetime from more flexible operation. Due to the complex geometry of the blade, an analytical solution for the stresses for a given load is not possible to obtain, so calibration is needed. A combination of strain measurement and numerical analysis is used to correlate the response from the strain gauges directly to the strains parallel to the trailing edge. The strain gauges are installed on the suction side of the blades, and close to the hub and shroud, and the calibration is done by applying known weights on the shroud using a tailor made blade fixture. The signal from the sensors is passed through a set of miniature amplifiers that fits in the hub of the model runner. The numerical setup is done in ANSYS Mechanical, and is set up to fully replicate the conditions of the physical setup. The results shows that the method is viable, however there is a challenge with the response, and thus required amplification, due to the stiffness of the runner blade material.

1. Introduction

As the energy production transitions towards more renewable sources such as wind- and solar power, a higher demand for flexible operation is put on existing power plants, since solar- and wind power is non-dispatchable. Given the

goal of reducing CO_2 emissions in the energy production sector, the remaining dispatchable power sources will need to vary their operation and power output even more to meet the demands on the grid. Hydro power is both highly dispatchable and a renewable energy source, meaning that it is well suited to fill the role of balancing the power grid as the output from wind- and solar power varies and the consumption goes up or down. In Norway, there are more than 1100 hydro power plants with an installed capacity of more than 1 MW [5]. The majority of these were designed for operation on a more or less constant power output and with a small number of load changes and start-stop cycles. The most common type of hydro turbine in use is the Francis turbine, and one major drawback of more off-design operation and start-stop cycles of these turbines is the increase in fatigue loading on the runner itself, meaning that a Francis turbine used for more flexible operation schemes than it was designed for initially might need more maintenance and have unexpected and costly failures.

Due to the complex geometry of the runner blades, a simple analytical calculation of the strain at a certain location on the blade is not possible. In order to apply strain in the blade a force is applied at a small contact point by the use of weights, but to get a figure on the actual strain at the location of the strain gauges a numerical replication of the setup is used. The results of the finite element method (FEM) analysis is then used as the input in the regression analysis and a relationship between the strain in the blade and the strain gauge output is determined. In order to transmit the sensor output a slip ring is used, and therefor the signal is amplified before transmission, meaning that the output measured will be in volts.

This paper will focus on the calibration setup, procedure, and results of the strain gauges mounted on the trailing edge of a model Francis runner blade. A pair of pressure transducers have also been installed and calibrated, but since a static calibration of pressure is relatively standardised, an in depth description of the setup and method used will not be presented.

2. Calibration setup and instrumentation

The flexibility and operational constraints of any Francis turbine are largely dependent on the hydrodynamic and structural characteristics of the turbine's runner. For that reason, one of the tasks in the HydroFlex project is to combine structural and fluid-flow simulations in one design tool, which will support the process of designing more flexible Francis turbines for the future grid-balancing needs. This tool is fully automated to perform simulations on series of operating conditions [8], and employs optimization methods in parametric environment [3]. In order to asses the accuracy of the numerical results, and later improve the tool, an experimental model runner was designed and installed in the Waterpower laboratory at NTNU. Therefore, apart from the standard efficiency measurements which will be performed to validate the hydraulic optimization

procedure, on-board measurements of the strain and dynamic loads on the runner blades will be performed over a wide operating range, during start/stop sequence, and rapid output adjustments.

2.1. Description of the model runner

According to the current state and possibilities in the laboratory, the measurement of the strain and dynamic loads on the runner blades is the most challenging task, and the experimental runner was primarily designed to fulfil several geometrical requirements that are expected to improve the measurements with strain gauges. These are:

- Fully supported blade from leading to trailing edge on both the hub and shroud sides. For validation purposes, this feature is expected to minimize uncertainties in the boundary conditions of the structural calculations.

- The runner blades must be as thin as possible to reduce the structural stiffness and provide larger blade deformation under the normal operating conditions of the turbine rig.

- The entire runner blade, especially the trailing edge, must have simple geometry that will make it easier for manufacturing with high accuracy and minimize the geometrical uncertainty. This resulted in low overall curvature of the blade, a trailing edge that is radial and without leaning, and a leading edge with only a small leaning.

- All blades must be detachable for easier instrumentation. Each blade section should have part of the hub and shroud as a single piece, which will be bolted together on common hub and shroud that are already available in the Waterpower laboratory.

- The runner must have a water-tight chamber inside the hub (center bushing) that will provide dry space for installation of on-board amplifiers and other electronics of the measuring chain.

The listed requirements pose significant geometrical restrictions in the design space of the runner, which will obviously affect and reduce the efficiency of the entire turbine. However, although the requirements for the hydraulic efficiency were relaxed and considered as secondary in the hydraulic optimization procedure, the tool was able to provide design which has efficiency on a comparable level with the original runner of the model turbine. The runner assembly is shown on Figure 1.

2.2. Description of the custom blade fixture

Because the blade sections have complex and unique geometry, a custom blade fixture was designed to provide with the needed support, orientation and load location for the calibration procedure. The loading of the blade during operation is expected to cause higher static strain values on the gauge mounted
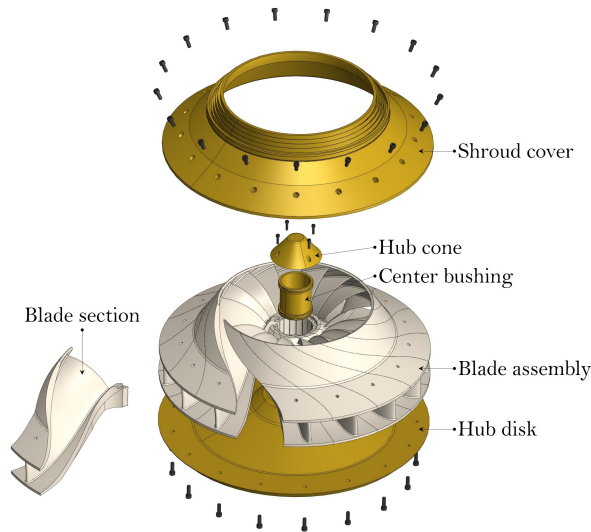
Figure 1. Exploded view of the runner assembly with isolated blade section. For simplicity, the on-board instrumentation is not shown.

close to the hub, and this was confirmed with initial high-fidelity CFD and FEA simulations. Due to this, the blade is bolted on the fixture using the bolt bores on the hub side of the section, and the loads were applied on the shroud side of the section. The orientation of the blade was adjusted so that the surface normal on the location where the loads are applied is directed vertically. The blade fixture is shown on Figure 2. The body of the blade fixture is over-dimensioned to provide with enough stiffness and stability during calibration, and was manufactured using 7075 Aluminium Alloy to reduce it's weight for easier handling in the laboratory. The pivot arm is made of S355 Non-Alloy Steel and is attached to the main body through a low friction SKF 607-2RSL closed ball bearing.

Both materials are selected to have slightly higher strength and slightly lower hardness than the material used for the blade section, which is JM7-15 Aluminium Bronze. The contact area between the arm and blade is dimensioned with enough margin to sustain twice the maximum required load before plastic deformation occurs on the arm. Under normal operating conditions of the model runner, the maximum principal elastic strains in the zone close to the trailing edges of the blades are nearly parallel to the trailing edge itself. This was confirmed by performing initial high-fidelity simulations within the HydroFlex project, and appears to be the case for other Francis turbines as well [1, 2, 9]. Therefore, the uni-directional strain gauges are also oriented parallel to the
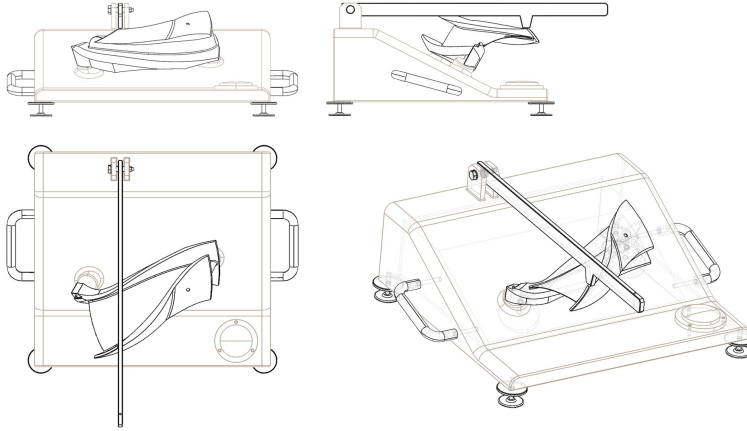
Figure 2. Orthographic and isometric views of the custom blade fixture designed for calibration of the strain gauges. The blade is bolted at two locations on the hub side and oriented to have a vertical direction of the surface normal at the location of the contact point with the arm. The fixture also has height adjustable legs and a spirit level gauge for horizontal adjustments before calibration.

trailing edge, and outside of the characteristic trailing edge chamfer. During the design stage of the strain calibrator, the numerical results revealed that the applied loads will result in tensile strains for the hub gauge and compressive strain for the shroud gauge. On the contrary, the blade loading under normal operation will produce only tensile strains for both gauges mounted on the suction side of the blade. This reversed effect during the calibration procedure is due to the location of the contact point on the blade section, and can be mitigated to some extent by a trial-and-error re-positioning. On the other hand, the ductile material of the blade has nearly equal elastic modulus in both tensile and compression directions, and during normal operation of the turbine both gauges will be well inside the linear range of the sensors. Therefore, the strain reversal effect is considered to be negligible, and the calibration curves for both gauges can be used for tensile and compression strains.

2.3. Planned experiment and measurement chain
The goal for the planned experiment is to measure the strain at the trailing edge near both the hub and shroud on two of the runner blades, as well as pressure near the leading edge of one blade. With the sensors being installed in the rotating runner, it was chosen to also amplify the sensor outputs before transmitting them through a slip ring mounted on the shaft in order to reduce the noise to signal ratio. From the slip ring, the signal is fed into a couple of

NI-cDAQ modules connected to a computer which also measures and records various inputs from the model test rig, as demonstrated in Figure 3. The recording is done in a custom LabVIEW program that also does some processing of the data on the fly. One alternative modification to the test setup which is under consideration is to reduce the amplification gain on the on-board amplifiers to reduce the noise stemming from the amplifiers them selves, and then increase the amplification after the slip ring to utilise the full analog range of the DAQ input. This might keep the noise to signal ratio from the slip ring low enough, while avoiding introducing too much noise from the miniature amplifiers.
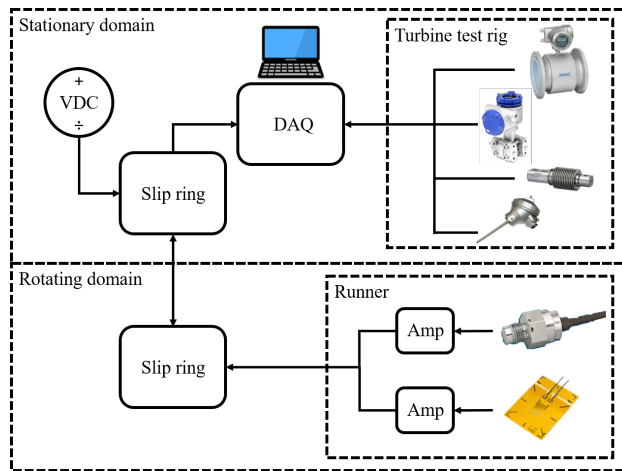
Figure 3. Illustration showing the measurement setup

2.4. Calibration setup and procedure

The calibration of the strain gauges is done by combining results from numerical simulations and measured results from the blade in the fixtureThe load is distributed with 10 points from minimum to maximum load starting with no weight applied, up to 15 kg hanging on the end of the arm of the fixture. It goes up in steps of 2 kg, except for near the end points. To check the repeatability of the measurements and any hysteresis, each point is taken four times, twice moving from a lower to a higher load, and twice moving from higher to lower. Due to the deformation of the arm itself it was found that a small horizontal force was applied to the blade as well as the intended vertical force, and the measurements would differ by an increasing amount as the applied weight increased, to the extent that the measured voltage differed by more than 10% at the highest load. One solution to this behaviour was to lubricate the contact surface between the shroud of the blade and the contact point of the

fixture arm and allow the horizontal displacement of the arm. In addition to the lubrication, it was found that tapping the blade with the handle of a small screw driver was also required to make the arm settle and drastically reduce the horizontal forces, and doing this reduced the discrepancy of the measured voltage at the max weight point to less than 1% for the hub gauge.

3. Numerical analysis

To obtain the values of elastic strain for both strain gauge locations, the dead weight strain calibration procedure was simulated in ANSYS Mechanical. For different weights applied as boundary conditions, steady-state structural simulations were performed with the primary goal to calculate the unidirectional elastic strains, while secondary goals were to calculate and control-check the equivalent stresses and total deformation of the blade.

3.1. Numerical setup

To simplify the procedure, the blade and arm were simulated separately, where the structural response of the arm was simulated first, and then the results were used as boundary conditions for the simulation of the structural response of the blade. For the arm, remote displacement support was used at the hinge to allow rotation only about the pivot axis (where a ball bearing is installed), while the contact point with the blade had a friction-less support in the vertical z-axis. Vertical force was applied equivalent to the different weights that were applied on the physical setup. For the blade, fixed support was used on the internal walls of the bolt bores and vertical force was applied on the contact point with the arm. On Figure 4 shown is a graphical representation of the numerical setup, together with contours of exaggerated total deformation relative to a non-deformed state. Gravitational effects in the form of steady-state inertial forces were also included for the blade and arm, using the local gravitational constant. In this type of analysis, the loads do not induce significant inertia effects and damping, assuming slow variation in time of the loads and the structure's response and time invariant end results [4]. All details of the FEA configuration in ANSYS Mechanical are given in Table 1.

The strains that are detected by the physical uni-directional strain gauges are averaged [10] and, for the simulation of this effect, surface elements are used in the setup to average over the area of the gauge. In that sense, the gauge is numerically represented as a single shell element with bounded contact to the surface of the blade, which provides with the averaging effect needed. Element type SHELL181 was used due to it's suitability for analysing thin shell structures and membranes [4], with stiffness set to zero to eliminate it's effects on the stiffness of the blade itself. Therefore, the thickness of the element is irrelevant because the element has only four nodes, however, to create the element grid the thickness was arbitrarily set to 20 μm. Additionally, local
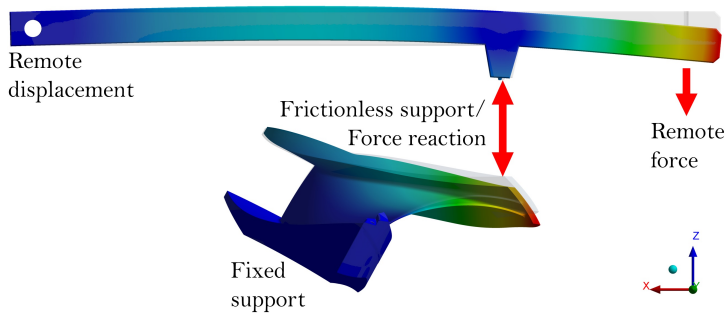
Figure 4. Boundary conditions for the structural setup. For demonstration purposes, the contours of the total deformation for the case with maximum weight applied is shown in scaled values, together with the non-deformed state. In true scale, the maximum deformation is less than 0.2 mm for the blade and the arm.

coordinate systems were defined for each surface element, allowing to calculate the strain in the correct direction of the gauge that is to be used for the calibration procedure.

Table 1. Configuration details in *ANSYS* Mechanical

	Blade	Strain gauge patch	Pivot arm
Analysis type	Static (steady-state)	Static (steady-state)	Static (steady-state)
Support	Fixed support	Bounded contact	Remote displacement, Friction-less support
Load	Normal force	Blade surface strain	Remote point force
Element size	0.63 mm	n/a	2 mm
Total elements	26512938	1	205159
Total nodes	36283766	4	301717
Element type	SOLID187	SHELL181	SOLID187
Grid type	Tetrahedral	Hexahedral	Tetrahedral
Solver type	Iterative	Iterative	Direct
Gravity	9.82146516 m/s^2	n/a	9.82146516 m/s^2
Temperature	20^oC	n/a	20^oC
Material	JM7-15 Aluminium Bronze	n/a	S355 Structural Steel
Young's modulus	118 GPa	n/a	210 GPa
Yield strength	300 MPa	n/a	335 MPa
Density	7600 kg/m^3	n/a	7850 kg/m^3
Mass	6.1423 kg	n/a	1.4757 kg

3.2. Estimation of uncertainty due to discretization

To estimate the discretization error in the structural simulations of the blade, the Grid Convergence Index (GCI) is used [6]. The GCI provides a uniform

procedure for reporting results from grid refinement studies, and is based on an error estimator derived from the Richardson Extrapolation method [7].
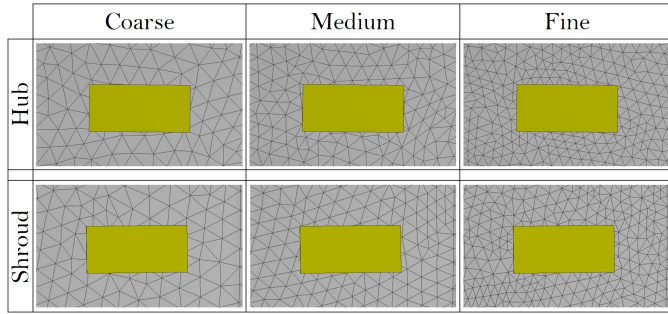
Figure 5. Detailed view of the computational grid close to the measuring zones of the strain gauges, and for the three grid resolutions used in the estimation of the discretization uncertainty. The strain calculated by the single element gauge (yellow) will be averaged upon the tetrahedral elements/nodes in contact.

Due to the complexity of the geometry, tetrahedral grid with control of the global element sizing h was used to generate three computational grids of size N, with refinement factor $r = h_{coarse}/h_{fine}$ of approximately 1.35. A detail view of the grid density around both gauges, and for all three grid sizes, are shown on Figure 5. The refinement was done globally, i.e., systematically in all three directions, in such way that the finest grid would end-up using the entire memory resource of a workstation with 128GB of RAM available. The strain values ϕ for the hub and shroud gauges are the key variables, and the results for the maximum weight applied were used to estimate the errors. As can be seen from the summary given in Table 2, the fine grid has error of less than 0,5% for both gauges, and all calculations needed for the calibration were done with this grid. The relations used to calculate all parameters in Table 2 are not repeated in this paper, and can be found in [6].

Table 2. Calculation of discretization error

Symbol	Hub strain gauge	Shroud strain gauge	Description	Unit
N_1	26.5M	26.5M	Grid size	-
N_2	10.78M	10.78M		-
N_3	4.39M	4.39M		-
r_{21}	1.3499	1.3499	Refinement factor	-
r_{32}	1.3493	1.3493		-
ϕ_1	109.9851	-16.6136	Microstrain	μm/m
ϕ_2	109.5226	-16.5656		μm/m
ϕ_3	108.5770	-16.4369		μm/m
p	2.3911	3.3014	Apparent order	-
ϕ_{ext}^{21}	110.4260	-16.6419	Microstrain	μm/m
e_a^{21}	0.42%	0.29%	Error	%
e_{ext}^{21}	0.40%	0.17%		%
GCI_{fine}^{21}	0.50%	0.21%	Grid convergence index	%

4. Calibration and uncertainty analysis

4.1. Calibration results
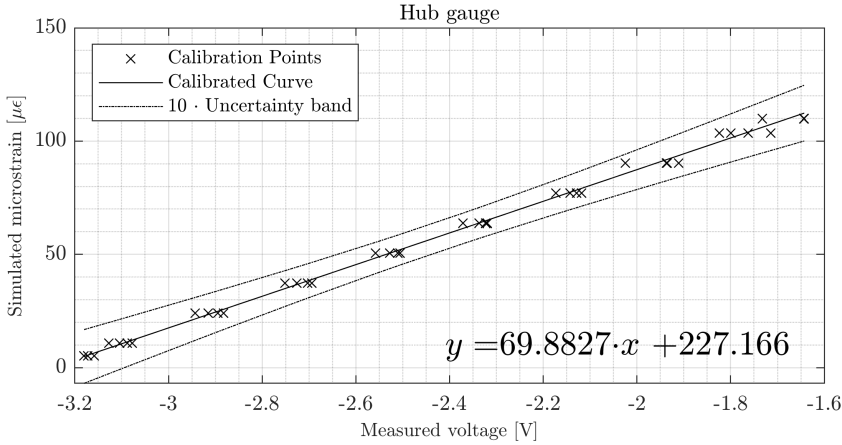
Figure 6. Calibration line, uncertainty bands and linear expression for the strain gauge near the hub side on the blade.

The results are also presented in Table 3 where X denotes the measured voltage, Y denotes the simulated strain, $f(X)$ denotes best fit, e_{tot} denotes the absolute total uncertainty, and f_{tot} denotes the relative total uncertainty. Subscript h refers to the strain gauge near the hub, and subscript s refers to the strain gauge near the shroud.
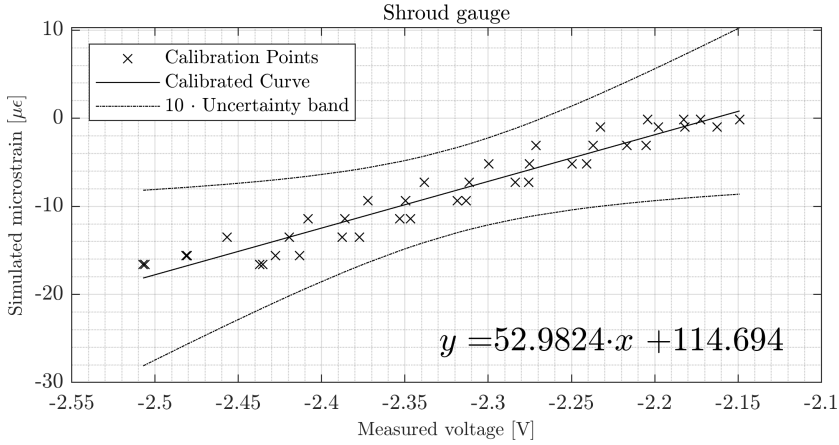
Figure 7. Calibration line, uncertainty bands and linear expression for the strain gauge near the shroud side on the blade.

4.2. Uncertainty analysis

To calculate the total uncertainty for each of the calibration points the root-sum-square of the random uncertainty and regression uncertainty was utilised. The random uncertainty was calculated by

$$e_{rand} = \frac{t_{\alpha/2} \cdot s}{\sqrt{N}} \tag{1}$$

where $t_{\alpha/2}$ is the t value with a confidence level set to $97,5\%$, s is the standard deviation of the sampled data for one point, and N is the total number of samples for said measurement. The regression uncertainty is calculated after finding the linear fit for the measured points by calculating the variation in both x and y direction individually, and both direction combined.

Table 3. Calibration data from the both strain gauges.

X_h [V]	Y_h [μm/m]	$f(X_h)$ [μm/m]	$e_{h,tot}$ [μm/m]	$f_{h,tot}$ [%]	X_s [V]	Y_s [μm/m]	$f(X_s)$ [μm/m]	$e_{s,tot}$ [μm/m]	$f_{s,tot}$ [%]
-3,172	5,164	5,475	1,178	22,81	-2,204	-0,120	-2,098	-0,733	610,66
-3,127	10,765	8,617	1,130	10,50	-2,232	-1,001	-3,593	-0,639	63,86
-2,943	24,016	21,474	0,947	3,94	-2,271	-3,086	-5,647	-0,538	17,43
-2,751	37,268	34,912	0,789	2,12	-2,299	-5,171	-7,145	-0,494	9,56
-2,558	50,520	48,393	0,690	1,37	-2,338	-7,256	-9,202	-0,489	6,75
-2,370	63,766	61,479	0,675	1,06	-2,372	-9,341	-10,986	-0,538	5,76
-2,173	77,016	75,279	0,750	0,97	-2,408	-11,425	-12,902	-0,632	5,53
-2,025	90,266	85,638	0,855	0,95	-2,456	-13,510	-15,475	-0,798	5,91
-1,799	103,520	101,406	1,064	1,03	-2,480	-15,596	-16,740	-0,890	5,71
-1,732	109,985	106,106	1,134	1,03	-2,506	-16,613	-18,087	-0,992	5,98
-1,732	109,985	106,093	1,134	1,03	-2,507	-16,613	-18,141	-0,997	6,00
-1,824	103,520	99,700	1,040	1,00	-2,481	-15,596	-16,779	-0,893	5,73
-1,937	90,266	91,780	0,931	1,03	-2,419	-13,510	-13,499	-0,667	4,94
-2,142	77,016	77,409	0,769	1,00	-2,385	-11,425	-11,720	-0,570	4,99
-2,337	63,766	63,848	0,681	1,07	-2,349	-9,341	-9,790	-0,500	5,36
-2,528	50,520	50,498	0,682	1,35	-2,311	-7,256	-7,773	-0,485	6,69
-2,725	37,268	36,686	0,772	2,07	-2,275	-5,171	-5,849	-0,530	10,26
-2,915	24,016	23,447	0,921	3,84	-2,237	-3,086	-3,828	-0,626	20,28
-3,104	10,765	10,207	1,106	10,28	-2,197	-1,001	-1,749	-0,756	75,57
-3,180	5,164	4,913	1,186	22,98	-2,182	-0,120	-0,949	-0,812	676,79
-3,172	5,164	5,492	1,177	22,81	-2,172	-0,120	-0,403	-0,852	709,64
-3,088	10,765	11,349	1,089	10,12	-2,181	-1,001	-0,907	-0,815	81,45
-2,894	24,016	24,892	0,903	3,76	-2,216	-3,086	-2,755	-0,690	22,37
-2,703	37,268	38,265	0,758	2,04	-2,249	-5,171	-4,495	-0,590	11,41
-2,510	50,520	51,704	0,678	1,34	-2,283	-7,256	-6,308	-0,515	7,10
-2,323	63,766	64,818	0,685	1,07	-2,318	-9,341	-8,142	-0,483	5,18
-2,129	77,016	78,372	0,778	1,01	-2,353	-11,425	-9,981	-0,505	4,42
-1,935	90,266	91,914	0,933	1,03	-2,387	-13,510	-11,807	-0,574	4,25
-1,762	103,520	103,966	1,102	1,06	-2,427	-15,596	-13,935	-0,694	4,45
-1,644	109,985	112,259	1,229	1,12	-2,435	-16,613	-14,338	-0,720	4,34
-1,642	109,985	112,357	1,230	1,12	-2,437	-16,613	-14,429	-0,726	4,37
-1,714	103,520	107,336	1,152	1,11	-2,413	-15,596	-13,164	-0,647	4,15
-1,911	90,266	93,596	0,955	1,06	-2,377	-13,510	-11,256	-0,549	4,07
-2,117	77,016	79,162	0,786	1,02	-2,346	-11,425	-9,641	-0,497	4,35
-2,319	63,766	65,073	0,686	1,08	-2,313	-9,341	-7,867	-0,485	5,19
-2,505	50,520	52,067	0,677	1,34	-2,275	-7,256	-5,873	-0,529	7,30
-2,694	37,268	38,872	0,753	2,02	-2,240	-5,171	-4,028	-0,614	11,89
-2,882	24,016	25,741	0,892	3,72	-2,205	-3,086	-2,141	-0,730	23,66
-3,077	10,765	12,124	1,078	10,01	-2,162	-1,001	0,116	-0,890	88,92
-3,158	5,164	6,420	1,163	22,53	-2,149	-0,120	0,831	-0,944	786,50

5. Conclusion

In the future, hydro turbines will be operated at off load condition, and this will reduce their lifetime due to fatigue loads. Therefore, it is crucial for an owner of turbines to know their remaining lifetime at all times. The remaining lifetime can be calculated from fatigue loads on the turbine, and this is the reason why this paper is focusing on the measurements of stress and strain in hydro turbine runners. In order to measure the of hydro turbines The calibration method in this paper represent a new method for calibration of strain gauges in Francis model turbines. The method of using numerical analysis of the strain for calibration has never been used by personnel at the Waterpower Laboratory at NTNU earlier. It is the lack of other alternatives that gave this method a chance. However, with high quality numerical results, it has proven to be a good alternative for future calibrations.

6. Acknowledgements

References

[1] Halvard Bjørndal, Trond Moltubakk, and Hans Aunemo. "Flow induced stresses in a medium head Francis runner – Strain gauge measurements in an operating plant and comparison with Finite Element Analysis". In: June 2001.

[2] Eduard Doujak and Markus Eichhorn. "An Approach to Evaluate the Lifetime of a High Head Francis Runner". In: 2016.

[3] Igor Iliev et al. "Optimization of Francis Turbines for Variable Speed Operation Using Surrogate Modeling Approach". In: *Journal of Fluids Engineering* 142.10 (Aug. 2020). 101214. ISSN: 0098-2202. DOI: `10.1115/1.4047675`. eprint: `https://asmedigitalcollection.asme.org/fluidsengineering/article-pdf/142/10/101214/6554501/fe\_142\_10\_101214.pdf`. URL: `https://doi.org/10.1115/1.4047675`.

[4] ANSYS Inc. *ANSYS Mechanical APDL product documentation*. Release 18.2. 2017.

[5] NVE. *Vannkraft*. 2022. URL: `https://www.nve.no/energi/energisystem/vannkraft/` (visited on 03/08/2022).

[6] "Procedure for Estimation and Reporting of Uncertainty Due to Discretization in CFD Applications". In: *Journal of Fluids Engineering* 130.7 (July 2008). 078001. ISSN: 0098-2202. DOI: 10.1115/1.2960953. eprint: `https : / / asmedigitalcollection . asme . org / fluidsengineering/article-pdf/130/7/078001/5491455/078001\_1.pdf`. URL: `https://doi.org/10.1115/1.2960953`.

[7] P. J. Roache. "Perspective: A Method for Uniform Reporting of Grid Refinement Studies". In: *Journal of Fluids Engineering* 116.3 (Sept. 1994), pp. 405–413. ISSN: 0098-2202. DOI: 10.1115/1.2910291. eprint: `https : / / asmedigitalcollection . asme . org / fluidsengineering/article-pdf/116/3/405/5531128/405\_1.pdf`. URL: `https://doi.org/10.1115/1.2910291`.

[8] Erik Tengs et al. "Fully automated multidisciplinary design optimization of a variable speed turbine". In: *IOP Conference Series: Earth and Environmental Science* 774.1 (June 2021), p. 012031. DOI: 10.1088/1755-1315/774/1/012031. URL: `https://doi.org/10.1088/1755-1315/774/1/012031`.

[9] Julian Unterluggauer, Eduard Doujak, and Christian Bauer. "Fatigue analysis of a prototype Francis turbine based on strain gauge measurements". In: *WASSERWIRTSCHAFT* 109 (Sept. 2019), pp. 66–71. DOI: 10.1007/s35147-019-0238-9.

[10] N. Younis and B. Kang. "Averaging effects of a strain gage". In: *Journal of Mechanical Science and Technology* 25 (Mar. 2011), pp. 163–169. DOI: 10.1007/s12206-010-1020-1.

Paper 3

Challenges with onboard strain measurements on a model Francis turbine runner
Kverno, J. O., Vefring, G. E., Iliev, I., Solemslie, B. W. and Dahlhaug, O. G.

Challenges with onboard strain measurements on a model Francis turbine runner

Johannes Kverno[1]*, Gaute Elde Vefring[1], Igor Iliev[2], Bjørn Winther Solemslie[3] and Ole Gunnar Dahlhaug[1]

[1] Department of Energy and Process Engineering, Norwegian University of Science and Technology, Alfred Getz' vei 4, 7034 Trondheim, Norway
[2] SINTEF Energi AS, Sem Sælands vei 11, 7034 Trondheim, Norway
[3] Departement of of Aquatic Biodiversity, Norwegian Institute for Nature Research, Høgskoleringen 9, 7034 Trondheim, Norway

* E-mail: `johannes.kverno@ntnu.no`

Abstract. As the world transitions towards more renewable energy sources, as a step to reduce the emissions of CO_2, intermittent and non-dispatchable sources like solar and wind will take up a larger proportion of the energy production. With more unregulated power in the energy mix, a higher demand is put on the rest of the energy production system. Hydropower is in a unique position as it is both renewable and a highly flexible energy source. The increased use of flexible operation of Francis turbines especially, puts a higher dynamic load on the runner components which as a consequence leads to a reduced lifetime. In this paper we present the experimental setup and results from a measurement campaign performed on a model of a low specific speed Francis runner. Onboard measurements with strain gauges at the trailing edge of two runner blades were performed. The experiments were conducted as a part of the HydroFlex project with the goal of validating numerical simulations and to gain a better understanding of the reduction of lifetime on Francis turbines due to higher fatigue loading from more flexible operation. The results shows that there were a significant drift of the mean strain over time during the measurement campaign, and a lower measured strain at BEP than expected when compared to numerical simulations. In this paper, the experimental setup, results and challenges encountered are presented.

1. Introduction
The European Union, and most other countries in the world, have committed to reduce the emission of CO_2 and cut down on the reliance on fossil fuels. Within the EU, this means that at least 32% of the electrical energy production must come from renewable sources by 2030 [1] and by 80% by 2050 [2]. Two of the major renewable energy sources is wind and solar, both of which are intermittent sources. Since the electrical grid must be balanced between production and consumption, the introduction of a large fraction of non-dispatchable energy sources to the grid mix can lead to instabilities and damage to connected components if no other action is taken. As a consequence, the remaining energy producers on the grid must adjust their power output more frequently to keep the grid stable, both as demand changes and as there are changes in the incoming energy from the intermittent sources. Hydropower in Europe is in a unique position being a well developed, highly flexible and renewable energy source. The most commonly used type of turbine in hydropower is the Francis turbine and the mean age of the large Francis turbines are around 50 years. They were originally designed for very steady operation pattern with relatively little changes in the load. Future operation of the turbines will require high flexibility, leading to more fatigue and damage to the units. The runner is the most vulnerable part of the Francis turbine. This paper is about fatigue loads in the runner blades of Francis turbines. In order to gain a better understanding of how the blades of a Francis turbine is loaded during start-stop, ramping and off-design conditions a set of strain gauges were mounted at the trailing edge of two neighbouring blades. The location of the strain gauges were selected to be as close as possible to the "hot spots" where the maximum static principal strains occur. Additionally, because the strain gauge provides an averaged value of the strain over the area of the strain gauge itself, and not at a single point, locations with large gradients should be avoided. For this purpose, fluid-structure interaction simulations were initially performed at several operating points within the HydroFlex project. According to the simulations, the location of the hot spots remains nearly fixed throughout the entire operating range of the turbine, and the expected dynamic stresses are relatively low in comparison to the static stresses for the tested head. The trailing edge is typically also where cracks and material failure tend to appear in prototype runners. A model turbine has been set up at the Waterpower laboratory.

2. Experimental setup
2.1. Test rig and turbine runner
The experiments were done on a Francis model test rig at the Waterpower laboratory, NTNU, with a setup compliant with the IEC 60193 standard [3]. The test rig is a low specific speed Francis model turbine with a runner outlet diameter of $0,349$m and a maximum rated head of 30m. The spiral casing consists of 14 stay vanes and 28 guide vanes, while the turbine runner is made up of 17 blades. An 8 pole 3-phase 315kW asynchronous generator is connected to the turbine shaft and

is used to control and maintain the rotational speed. Control and measurement of the test rig is handled by a National Instruments compactRIO and LabVIEW system. The turbine runner used for the experiments is the Francis-101 (F101) which was tailor made for the HydroFlex project [4] and the experiment itself. The runner blade design was optimised for onboard measurements to compare and validate numerical simulations with the experimental results as the key objective. The runner dimensions were also constrained by the existing spiral casing and covers which are a scaled down model of the Tokke Power Plant [5], and it has the same external dimensions as the Francis-99 (F99) research turbine [6]. Another important design criteria was to maintain a similar efficiency characteristic as the F99 runner and with the best efficiency point (BEP) being at the same point of operation. While the leading edge (LE) of the blades were optimised solely with the hydraulics in mind, the trailing edge (TE) were not. The TE were made as thin as possible to increase the response of the strain measurements and with a radial edge [7]. The entire length of the runner blades also had to be firmly fixed within the blade sections (illustrated in Figure 1). It was important to have control over the contact surfaces and friction between the blade sections and the hub disk and shroud cover, so no unattached blade sections extends beyond the blade section. The runner is also designed on the same platform as the Francis-100 (F100) runner developed in the HydroCen research project [8, 9] at the Waterpower Laboratory. So while F-101 shares the same hub disk and shroud cover with the F100 runner, the blades can be designed with a lot of freedom since the hydraulic surfaces of the hub and shroud also is a part of the blade sections. The design itself was made with the same quadratic surface model
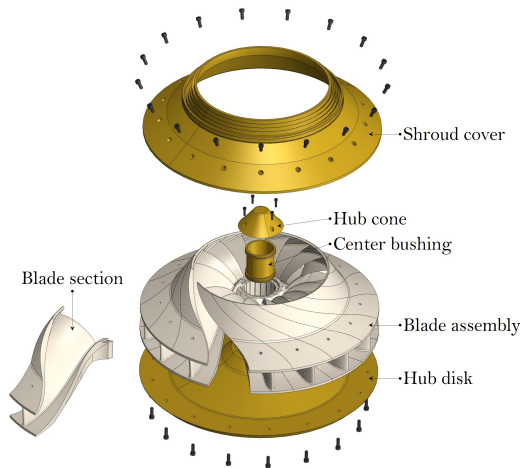

Figure 1: Exploded view of the F101 runner used for the experiments showing its method of assembly.

as the F100, but with 12 free parameters instead of the original 15 [7]. With the design of the runner assembly, relatively little space was left for instrumentation on board, with the only dry location with room for electronics being within the center bushing, as seen in Figure 1. This packing constraint limited the number of onboard sensors and amplifiers that could be fitted.

2.2. Experiment setup

The test rig includes a whole suite of sensors to measure flow rate, pressures, rotational speed, level of dissolved oxygen in the water, shaft bearing friction torque, etc. In addition, pressure sensors were mounted on the rig, two on the draft tube cone near the outlet of the runner separated by 180°, and three on the top cover in the vaneless space between the guide vanes and runner inlet. On board the runner there were two pairs of strain gauges mounted on the suction side of the TE near the hub and shroud, on two neighbouring blades. The transmission of the data and power supply from the rotating to stationary domain was through sliprings mounted on the turbine shaft. Sliprings were chosen to avoid the issue of data synchronisation when having two individual and separated sets of measurement chains. In order to minimise the noise to signal ratio, amplification of the sensor output were done onboard as well. After the slipring the signal were fed into a DAQ module placed near the rig, also illustrated in Figure 2.
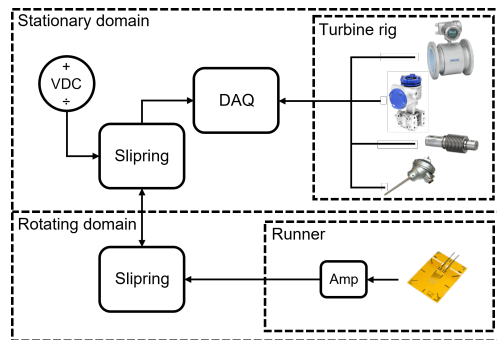
Figure 2: Illustration of the measurement chain as used in the experiments

2.3. Sensors and calibration

The strain gauges chosen for the experiment was the 1-LY41-6/350 1 grid linear strain gauge by HBM [10]. This choice was made due to its relatively small grid size and similar thermal expansion properties as the runner blade material itself. The exact positioning was chosen based on numerical simulations of where the strain gradients would be as low as possible, but still with a high enough strain to capture it to minimise the uncertainty. The direction of the strain gauges

were parallel to the TE, which is in line with the direction of the maximum principal static strains. Since the strain gauges were single grid gauges the rest of the Wheatsone bridge was completed in the hub next to the amplifiers with three high precision 350Ω metal foil resistors [11]. One goal of this measurement campaign was to get a better understanding of the actual stress in the blades at the location of the strain gauges. In order to enable the validation of the numerical simulations that were performed on the same turbine runner. To get the stress from the measured strain, a calibration rig and procedure was developed where a series of loads would be applied to the blade and the response and amplified output from the chain was recorded. Then, the same set of loads were set up in a numerical simulation and the material stress in the same location and direction as the strain gauges were stored, giving a calibration from measured volts to strain. More details and results of the strain gauge calibration will be the topic of another upcoming publication. The calibration of the rest of the sensors attached on the Francis test rig were performed in compliance with the IEC60193 standard [3].
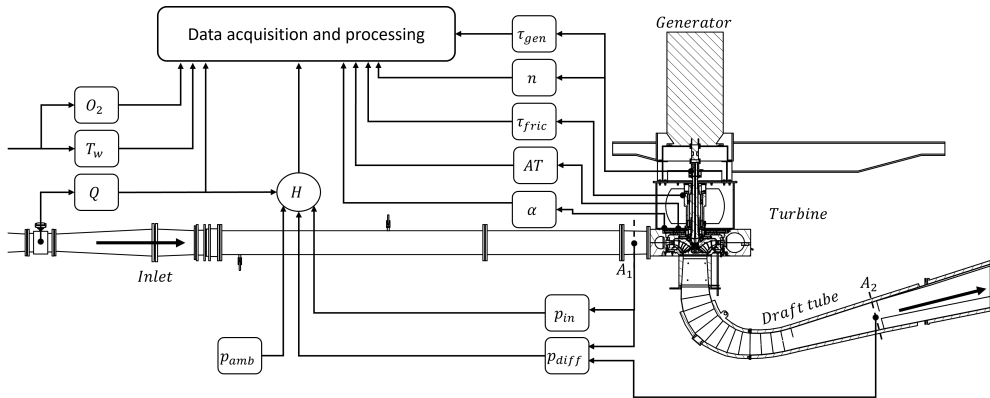
Figure 3: Overview of the test rig and the location of the measurements.

2.4. Signal conditioning and acquisition

The selected amplifiers were Mantracourt ICA3H embedded strain gauge analouge amplifiers [12]. The ICA3H uses a bipolar DC power supply of ±14V with a bridge excitation voltage of 5V and an output of ±10V. The amplifier gain had to be increased from the default factory configuration in order to get a large enough signal response from an applied load on the blade. In the end, it was decided that a $1026\times$ gain was the best compromise, with a signal response in the 10^0V order of magnitude and still small enough to allow some temperature related drift without clipping the signal.

(a) Outlet of turbine runner

(b) Vaneless space between the wicket gate and turbine runner

Figure 4: Detailed view of the location of strain gauges (a) and pressure sensors (b) mounted on the turbine test rig

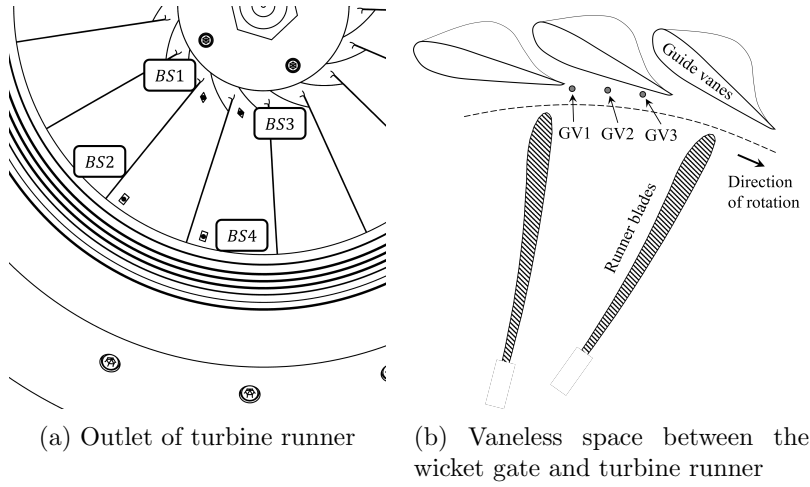| Measurand	Symbol	Unit	Manufacturer	Uncertainty	Sampling rate
Flow rate	Q	[m^3/s]	Krohne	$\pm 0,128\%$	10Hz
Inlet	p_{in}	[kPa]	GE Druck	$0,059$kPa	5000Hz
Differential	p_{diff}	[kPa]	Fuji	$0,066$kPa	5000Hz
Ambient	p_{amb}	[kPa]	Vaisala	$\pm 0,025$kPa	1Hz
Vaneless space	$GV\#$	[kPa]	Kulite	$0,29$kPa	5000Hz
DT pressure	$DT\#$	[kPa]	Kulite	$0,030$kPa	5000Hz
Blade strain	$BS1$	[μm/m]	HBM	$1,2307\mu$m/m	5000Hz
	$BS2$	[μm/m]	HBM	$0,9971\mu$m/m	5000Hz
	$BS3$	[μm/m]	HBM	$1,2641\mu$m/m	5000Hz
	$BS4$	[μm/m]	HBM	$0,7639\mu$m/m	5000Hz
Water temp.	T_w	[°C]	Siemens	$\pm 0,005\%$	10Hz
Shaft torque	τ_{gen}	[Nm]	HBM	$0,003\% M_{Nom}$	50Hz
Friction torque	τ_{fric}	[Nm]	Hottinger	$0,83$Nm	5000Hz
Speed of rotation	n	[RPM]	HBM	$\pm 1,5$RPM	50Hz
Axial thrust	AT	[kN]	Fuji	$\pm 0,1\% Fs$	5000Hz
Guide vane angle	α	[°]	Stegmann	$\pm 0,05°$	1Hz
Dissolved oxygen	O_2	[mg/l]	Xylem Ysi	$\pm 0,1$mg/l	10Hz

Table 1: List over all sensors used during the experiment, their uncertainties and sampling rate.

3. Results and validation

The mean measured strain at $BS1$ is shown in Figure 5. Similar results were also seen in the results from $BS2$ and $BS3$, while $BS4$ had a failing connection or wire which caused it to drift out of the range of the measurement equipment. The standard deviation of the measured signal were in the range of $0,35\mu\epsilon$ to $2,3\mu\epsilon$ for all strain gauge measurements.

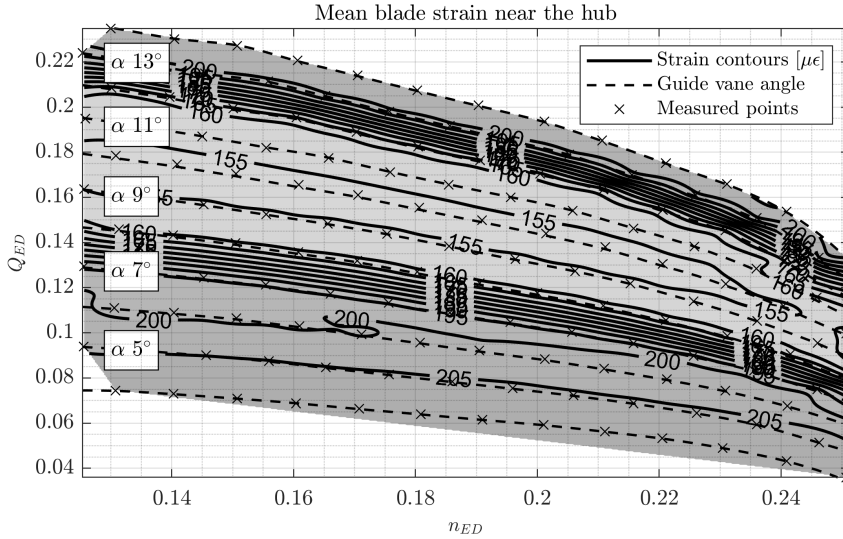In order to confirm the repeatability and validity of all the measurements through

Figure 5: Contour of the measured mean blade strain near the hub ($BS1$).

out the measurement campaign, one operating point was chosen as a reference point and repeatedly logged at the beginning and end of each day as well as in between measurement series. This point was set to be at n_{ED} of $0,18$, α of $10°$ and H_n of 12m. In total, thirteen reference point repetitions were measured in relation to the results presented in this paper. The strain gauge measurements for the reference points can be seen in Figure 6, note $BS4$'s deviation from the general trend. As a result of $BS4$'s deviation none of the results from that gauge were considered during the post processing.

If the drift is sorted by which guide vane angle each reference was taken before instead of chronologically, illustrated in Figure 7, it becomes clearer how the drift skewed the data with the lowest mean strain at $10°$ opening as that was the first measurement series taken during the campaign. Figure 8 shows the results from adjusting for the drift of the strain gauges over the time of measurement. The adjustment is done by subtracting the mean strain with the drift measured at the repeated reference point, meaning that the values are no longer absolute but the difference between the measured strain and the mean strain at BEP for that
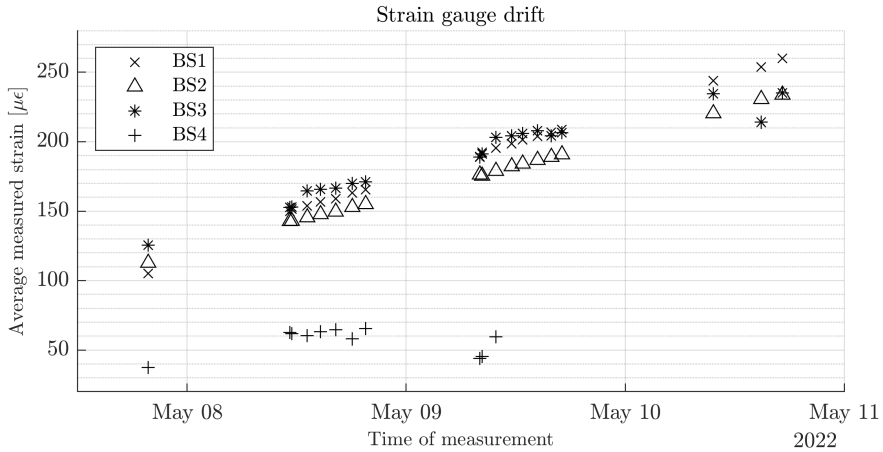
Figure 6: Measured drift over the course of the experiment at the reference point.
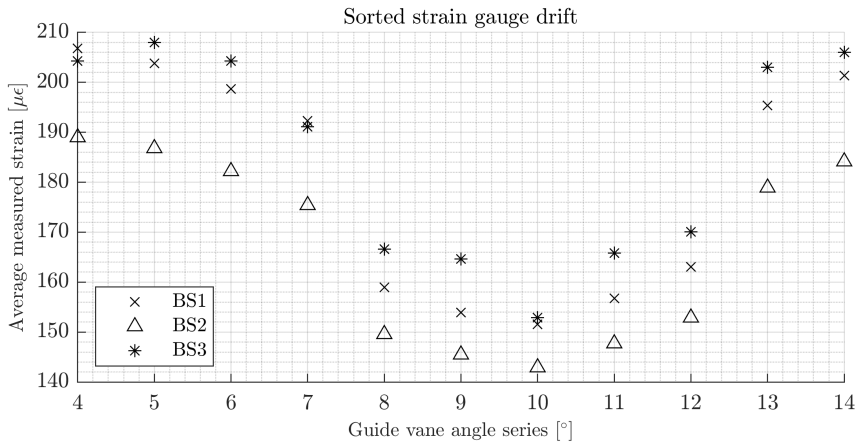
Figure 7: Measured drift sorted by which guide vane opening series each point preceded.

point in time. When compensating for the drift, there is no similarity between the measurements from $BS1 - BS3$. Some difference in the mean strain is to be expected between the gauges near the hub and shroud ($BS1$ & $BS2$), but similar trends would be expected when comparing two hub mounted gauges for instance ($BS1$ & $BS3$), as seen in Figure 9. SSO, or synchronous speed operation is taken at a fixed n_{ED} of $0, 18$. VSO, or variable speed operation is an operation scheme which follows the line of highest hydraulic efficiency for any guide vane opening. At the beginning and end of each day measurements were done while the runner was stationary and submerged as well as operating at BEP, so the static strain

Figure 8: Contour of the apparent strain when compensating for the drift ($BS1$).

Figure 9: Comparing the strain measurements near the hub on both blades ($BS1$ & $BS3$)

at BEP operation can be found by calculating the difference between BEP and stationary. The difference is presented in Table 2.

Table 2: Measured change in strain between unloaded and BEP load through out the campaign

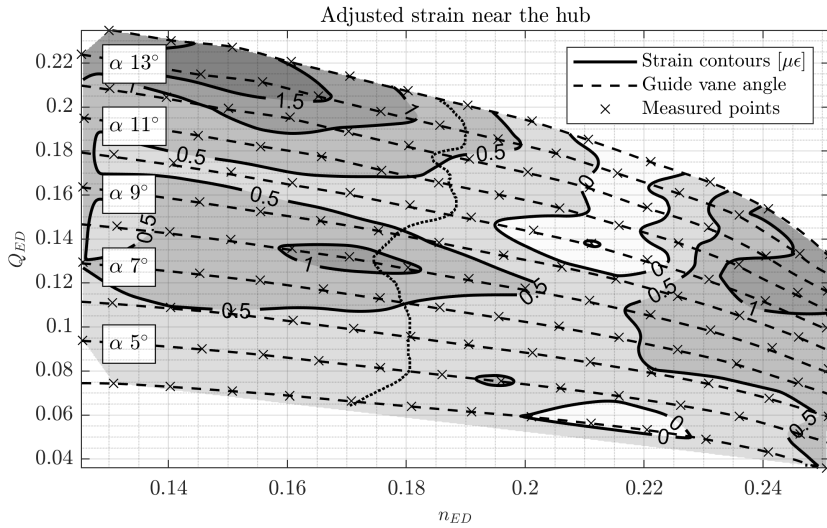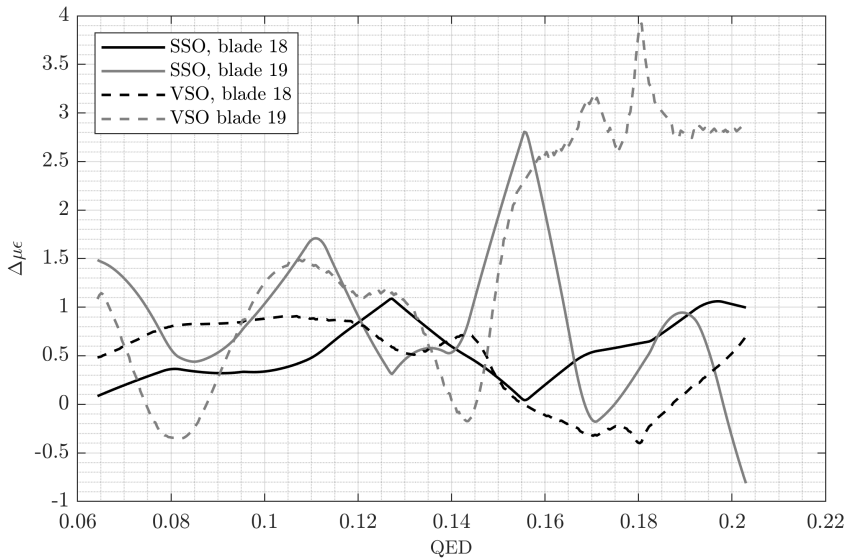| Time between points	Strain difference		
	BS1	BS2	BS3
00:07:39	-0,59511	0,897605	-1,86688
00:05:46	-0,61241	0,673372	-1,83541
00:11:52	-1,59027	0,591596	-4,27784
00:08:44	-0,71338	0,576053	-3,98752
00:15:45	-1,17821	0,402121	-6,54958
00:05:59	-0,33918	0,942753	-5,8496

4. Discussion, conclusion and further work

4.1. Drift and systematic error

At first glance looking at Figure 5 it might seem like there is an increase in the mean strain on the runner blade when moving away from a guide vane opening of 10°. The contour lines also seem to almost perfectly follow the guide vane lines, i.e. not being dependent on the n_{ED} at all. This result however turned out to be an artefact caused by the order of which the measurements were performed, and the same trends could be seen from the reference measurement points taken throughout the campaign. With the recorded reference points, it was attempted to offset the measured values at each point with the corresponding reference data and see if there were any trends in the measured strain but since the mean strain at any point was unknown, the adjusted values is close to zero, and are almost one order of magnitude less than the standard deviation of the raw signal. The primary cause of the drift seen through the experiment is assumed to be a result of the water temperature slowly increasing, starting at $14, 7$°C and reaching $16, 5$°C by the end of the campaign. The increase in water temperature is suspected to be a result of both the water running through uninsulated pipes and tanks in a room with a higher air temperature than what the water had, and the mechanical losses in various parts of the system adding some extra heat.

4.2. Electrical noise

Another issue encountered during the measurement campaign was excessive noise on the amplified onboard signals. This noise would only appear when the generator was turned on, so the source is believed to be the alternating current in the machine and cables. The main frequencies seen in the noisy signals were harmonics of the frequency of the AC generator, and the observed level of noise in the signal increased by $3 - 4 \times$ when the generator turned on.

4.3. Comparison with numerical simulation

Some preliminary structural simulations of the runner were performed early on in HydroFlex, and from those the expected strain at the locations of the gauges was extracted for operation at BEP. During the measurement campaign data was also recorded with the runner stationary but still submerged in water shortly after reference measurements at BEP, meaning that the difference in mean strain from stationary and BEP operation should be the absolute strain at BEP. However, this difference was an order of magnitude lower than what was seen in the simulations. The measurements were repeated multiple times throughout and there is a significant difference in between each of them, which would at least indicate that the experimental result is non conclusive.

4.4. Further work

The next step in this process now is to identify where in the measurement chain the noise is picked up, i.e. if it is from the cables running through the turbine shaft, before the amplification, or maybe even from the power source feeding the amplifiers. Secondly, more sensitive strain gauges are needed, as the mean value of the strain seems to be relatively unaffected by changing loads compared with the standard deviation of the signal. Finally, a better way to compensate for temperature related drift since there is no practical way to control the water temperature in the test rig at the Waterpower Laboratory. The compensation can either be by having some variability of one or more resistors in the Wheatstone bridge, or record the drift more frequently when the turbine runner is stationary but still submerged.

References

[1] European Commission. *A policy framework for climate and energy in the period from 2020 to 2030.* 2014.

[2] European Commission. *A clean planet for all. A European strategic long-term vision for a prosperous, modern, competitive and climate neutral economy.* 2018.

[3] International Electrotechnical Commission. *60193:2019 Hydraulic turbines, storage pumps and pump-turbines - Model acceptance tests.* 2019.

[4] Norwegian University of Science and Technology. *HydroFlex - Increasing the value of Hydropower through increased Flexibility.* URL: https://www.h2020hydroflex.eu/ (visited on 20/01/2023).

[5] Einar Kobro, Torbjørn Kristian Nielsen and Ole Gunnar Dahlhaug. 'Data analysis from onboard francis model runner pressure measurements'. In: *13th International Symposium on Transport Phenomena and Dynamics of Rotating Machinery 2010, ISROMAC-13.* 2010, pp. 98–103.

[6] Norwegian Hydropower Centre. *Francis-99.* URL: https://www.ntnu.edu/nvks/francis-99 (visited on 20/01/2023).

[7] Igor Iliev. *HydroFlex D3.4 - Hydraulic and mechanical design of the Francis model turbine.* Tech. rep. 2020.

[8] Norwegian University of Science and Technology. *HydroCen.* URL: https://www.ntnu.no/hydrocen (visited on 20/01/2023).

[9] Igor Iliev et al. 'Optimization of Francis Turbines for Variable Speed Operation Using Surrogate Modeling Approach'. In: *Journal of Fluids Engineering* 142.10 (Aug. 2020). 101214. ISSN: 0098-2202. DOI: 10.1115/1.4047675. eprint: https://asmedigitalcollection.asme.org/fluidsengineering/article-pdf/142/10/101214/6554501/fe_142_10_101214.pdf. URL: https://doi.org/10.1115/1.4047675.

[10] Hottinger Baldwin Messtechnik GmbH. *Strain Gauges - Absolute precision from HBM.* Datasheet. 2018. URL: https://pdf.directindustry.com/pdf/hbm-test-measurement/hbm-estrain-gauge-catalog/6017-266731.html#open614644 (visited on 20/01/2023).

[11]   VPG Vishay Foil Resistors. *High precision foil resistor with TCR of $\pm 2.0 ppm/^\circ C$, tolerance of $\pm 0.005\%$ and load life stability of $\pm 0.005\%$.* Datasheet. 2015. URL: `https://foilresistors.com/docs/63001/63001.pdf` (visited on 26/01/2023).

[12]   Mantracourt. *ICA emedded strain gauge analogue amplifiers.* 2018. URL: `https://www.mantracourt.com/userfiles/documents/ica_user_manual.pdf` (visited on 26/01/2023).

Paper 4

Onboard measurements with strain gauges on a model Francis runner
Kverno, J. O., Iliev, I., Solemslie, B. W. and Dahlhaug, O. G.
To be submitted 2023

Part III

Appendix

Slip ring pinout

In this section, the pinout, wire colours and duty of each lead to the slip ring is listed. The slip ring had two wire harnesses of 12 wires in each, so for practical purposes, and to avoid the risk of connecting power to the wrong set of wires and damaging the equipment, they were given different gendered connectors. In the table, when speaking of *Com*, we're refering to the 0V line from the power supply, and the negative or return end of the signal wires. The thinking behind spreading the power supply over several channels was that it would help reduce interference from the slip ring itself, which perhaps could have affected the amplifiers, and there were plenty of channels to spare anyway.

Table 1: Pin numbering and wire colours of the stationary side of the slip ring.

Pin #		Slip ring wire colour	Male connector Black harness	Female connector Red harness
2		Red	Sh1	+ 15
9		Black	Com	Com
3		Green	Ss1	- 15
10		Blue	Com	Com
4		White	Sh2	+ 15
11		Brown	Com	Com
5		Sky blue	Ss2	- 15
13		Gray	Com	Com
6		Yellow	Sref	+ 15
14		Purple	Com	Com
7		Beige	-	- 15
15		Orange	-	Com
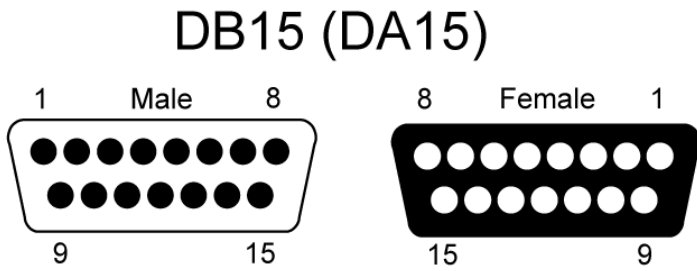
Figure 1: Pin numbering of the DB15 connector used from the slip ring.

MATLAB functions

In this appendix, a couple of the most important and used self made MATLAB functions for the post processing is presented. They work by taking in the raw data as saved by the Francis logger LabVIEW program, converted to a .mat file where the struct contains two fields, *Measurements* with the raw measured data, and *Processed* with the calculated data from the logger.

```matlab
function [avg,nsAvg] = JKaverageFrancis(signal,sensor)
%JKaverage Calculates the averages from the Francis rig
%
% SYNTAX
% avg = JKaverageFrancis(signal)
% avg = JKaverageFrancis(signal,sensor)
% [avg,nsAvg] = JKaverageFrancis(___)
%
% INPUT
% signal: Measurement field containing all the sensor
%   data
% sensor: (Optional) Name of the sensor data to be
%   averaged
%
% OUTPUT
% avg: Averaged values
% nsAvg: (Optional) Non-scaled averaged values
%
% DESCRIPTION
%   Made for the structure of the output from the
%   VKL-Francis logger.
%
% avg = JKAVERAGEFRANCIS(signal) returns the averages
%   scaled according to the calibration constants entered
%   into the logger.
%
% avg = JKAVERAGEFRANCIS(signal,sensor) returns the averages
%   of the specified sensor.
%
% [avg,nsAvg] = JKAVERAGEFRANCIS(___) returns the averages
%   both scaled and non-scaled.
%
% See also: Documentation on MEAN.
%

switch nargin
    case 1
        fields = fieldnames(signal);
        fields(find(strcmp(fields, 'name') + ...
 strcmp(fields, 'properties'))) = [];
        index = find(strcmpi(fields, 'RPM'));
        fields(end+1) = fields(index);
        fields(index) = [];
        index = find(contains(fields, 'timestamp'));
        fields(index) = [];
        exclusion = ...
 {'FlowRate', 'WaterTemperature', 'DissolvedOxygen',...
            'WaterTemperature', 'GeneratorTorque'};
        for i=1:numel(exclusion)
            index(i,1) = find(strcmpi(fields, exclusion{i}));
        end
        fields(index) = [];
```

1

116

```matlab
        for i=1:size(fields,1)-1
            if isfield(signal.(fields{i}), 'properties')
                avg.(fields{i}).value = mean(signal.
(fields{i}).Values);
                if strcmpi(fields(i), 'GenTorque')
                    avg.(fields{i}).value = abs(avg.
(fields{i}).value);
                end
                if nargout >1
                    scale = signal.(fields{i}).properties.FDB_Scale;
                    offset = signal.(fields{i}).properties.FDB_Offset;
                    nsAvg.(fields{i}).value = (avg.(fields{i}).value -
 offset)/scale;
                end
                if isfield(signal.
(fields{i}).properties, 'wf_start_time')
                    avg.(fields{i}).startTime = datetime(signal.
(fields{i}).properties.wf_start_time,...
                        'InputFormat', 'dd-MMM-yyyy HH:mm:ss.SSS');
                end
            else
                if strcmpi(fields(i), 'VISAPatm')
                    avg.(fields{i}).value = mean(signal.
(fields{i}).Values)*1e3;
                elseif strcmpi(fields(i), 'NPSVPatm')
                    avg.(fields{i}).value = mean(signal.
(fields{i}).Values)*1e3;
                else
                    avg.(fields{i}).value = mean(signal.
(fields{i}).Values);
                end
            end
            avg.(fields{i}).std = std(signal.(fields{i}).Values);
            avg.(fields{i}).N = length(signal.(fields{i}).Values);
            t = tinv(0.975,avg.(fields{i}).N);
            avg.(fields{i}).e_r = t * avg.(fields{i}).std / avg.
(fields{i}).N;
            avg.(fields{i}).f_r = avg.(fields{i}).e_r / avg.
(fields{i}).value;

        end
        rpm = signal.RPM.Values;
        if isfield(signal.RPM, 'properties')
            speedTime =
 datetime(signal.RPM.properties.wf_start_time,...
                'InputFormat', 'dd-MMM-yyyy HH:mm:ss.SSS');
        end
        avg.rpm.value = mean(rpm);
        if exist('speedTime', 'var')
            avg.rpm.startTime = speedTime;
        end
        avg.rpm.std = std(rpm);
        avg.rpm.N = length(rpm);
```

2

117

```matlab
            t = tinv(0.975,avg.rpm.N);
            avg.rpm.e_r = t * avg.rpm.std / avg.rpm.N;
            avg.rpm.f_r = avg.rpm.e_r / avg.rpm.value;
            if nargout>1
                nsAvg.rpm.value = mean(rpm);
            end
        case 2
            fields = sensor;
            avg.(fields).value = mean(signal.(fields).Values);
            avg.(fields).std = std(signal.(fields).Values);
            avg.(fields).N = length(signal.(fields).Values);
            t = tinv(0.975, avg.(fields).N);
            avg.(fields).e_r = t * avg.(fields).std / avg.(fields).N;
            avg.(fields).f_r = avg.(fields).e_r / avg.(fields).value;
            if nargout>1
                scale = signal.(fields).properties.FDB_Scale;
                offset = signal.(fields).properties.FDB_Offset;
                nsAvg.(fields) = (avg.(fields) - offset)/scale;
            end
end
end


testData =

  struct with fields:

            name: 'SynchOp 20m'
    Measurements: [1×16 struct]
       Processed: [1×16 struct]
        Averages: [1×16 struct]
```

Published with MATLAB® R2020a

118

The *JKaverageFrancis* function takes in the measured data struct from the logging program an returns the average for each sensor time series. It will also return the standard deviation, number of samples and the random uncertainty.

```matlab
function [calc] = JKefficiencyFrancis(avg)
%JKefficiencyFrancis Calculates the hydrauulic efficiency
%
% SYNTAX
% calc = JKefficiencyFrancis(data)
%
% INPUT
% avg: Averaged values from all the sensors.
%
% OUTPUT
% calc: CalculaTED.value values of the averaged input.
%
% DESCRIPTION
%   Made for the structure of the output from the
%   Francis logger.
%
% calc = JKEFFICIENCYFRANCIS(avg) tags on the calculaTED.value
%   values required to calculate the hydraulic efficiency
%   of a model turbine in the Francis rig at the
%   Waterpower Laboratory.
%
% See also: Documentation on the VKL wiki (<a href="Wiki:
% web('www.ntnu.no/wiki/display/vkl/FO-01-Procedure+for+computing
+physical+quantities+for+models+in+the+Francis+Turbine+Test
+Rig')">FO-01</a>) on the calulation of the physical qunatities.
%

A(1) = 0.0872; A(2) = 0.236033;
z(1) = 2.067;   z(2) = 0.9955;
d22 = 0.349;
g = 9.821465;

patm = fieldnames(avg);
patm = patm{find(contains(patm, 'Patm'))};


    % Water density at the inlet [kg/m3]
RhoIn.value = 1000/(1-4.6699e-10*avg.InletPressure.value) ...
    + 8e-6*(avg.Twater.value - 4 +
 2.1318913e-7*avg.InletPressure.value).^2 ...
    - 6e-8*(avg.Twater.value - 4 +
 2.1318913e-7*avg.InletPressure.value).^3;
RhoIn.e_r = 0.2;
    % Absolute inlet pressure [kPa]
Pin.value = (avg.InletPressure.value + avg.(patm).value) -
 (RhoIn.value*g*z(1))/1000;
Pin.e_r = sqrt(avg.InletPressure.e_r^2+avg.(patm).e_r^2 +
 RhoIn.e_r^2);

    % Absolute outlet pressure [kPa]
Pout.value = Pin.value - avg.DifferentialPressure.value;
```

```matlab
    % Water density at the outlet [kg/m3]
RhoOut.value = 1000/(1-4.6699e-10*Pout.value*1000) +...
    8e-6*(avg.Twater.value - 4 + 2.1318913e-7*Pout.value*1000).^2 -...
    6e-8*(avg.Twater.value - 4 + 2.1318913e-7*Pout.value*1000).^3;

    % Averaged density of the water [kg/m3]
Rho.value = RhoIn.value*.5 + RhoOut.value*.5;

    % Head.value calculation [mWc]
c1.value = avg.Flow.value/A(1);
c2.value = avg.Flow.value/A(2);
Head.value = (avg.DifferentialPressure.value +...
    .5*(Rho.value*(c1.value.^2 - c2.value.^2)))/(Rho.value*g);

    % Power calculation [kW]
Phyd.value = Rho.value*g*Head.value*avg.Flow.value*1e-3;
Pmech.value = avg.rpm.value * (pi/30)*...
    (avg.GenTorque.value + avg.FrictionTorque.value)*1e-3;

    % Hydraulic efficiency calculation [-]
eta.value = Pmech.value/Phyd.value;

    % Specific speed of rotation
nED.value = (avg.rpm.value*d22)/(60*sqrt(Head.value*g));

    % Specific Flow.value rate
QED.value = avg.Flow.value/((d22.^2)*sqrt(Head.value*g));

    % Specific torque
TED.value = (avg.GenTorque.value + avg.FrictionTorque.value)/
(Rho.value*g*Head.value*(d22^3));

    % Specific power
PED.value = (1e3*Pmech.value)/
(Rho.value*(d22^2)*g*Head.value*sqrt(Head.value*g));


calc.Pin = Pin;
calc.Pout = Pout;
calc.Rho = Rho;
calc.Head = Head;
calc.Phyd = Phyd;
calc.Pmech = Pmech;
calc.nED = nED;
calc.QED = QED;
calc.TED = TED;
calc.PED = PED;
calc.eta = eta;

end


testData =
```

2

121

```
struct with fields:

          name: 'SynchOp 20m'
  Measurements: [1×16 struct]
     Processed: [1×16 struct]
      Averages: [1×16 struct]
    Calculated: [1×16 struct]
```

Published with MATLAB® R2020a

The *JKefficiencyFrancis* function takes the averaged data from the previous function and returns the calculated values, such as head, density, power, non dimensional factors, and efficiency.

```matlab
function [pxx,f] = JKwelch3(varargin)
% JKwelch3 combines the pwelch function with the FDB logger data
%  structure
%
% SYNTAX
%   [pxx,f] = JKwelch3(signal)
%   [pxx,f] = JKwelch3(signal,...,'window',<arg>)
%   [pxx,f] = JKwelch3(signal,...,'fr',<arg>)
%   [pxx,f] = JKwelch3(signal,...,'noverlap',<arg>)
%   [pxx,f] = JKwelch3(signal,...,'fN',<arg>)
%
% INPUT
% signal: Measured signal and properties
% window: (Optional) Window function name
% fr: (Optional) Wanted frequency resolution
% noverlap: (Optional) Degree of window overlap from
%          0 to 1
%   fN: (Optional)  Normalisation frequecy, e.g. the
%       rotational frequency of the runner.
%
% OUTPUT
% pxx: Amplitude vector
% f: Frequency vector
%   NOTE: If no output variable names are given the
%         defaults pxx and f will be used, overwriting
%         anything in the workspace.
%
% DESCRIPTION
%   Made for the structure of the output from the
%   FDB-Francislogger.
%
% [pxx,f] = JKWELCH3(signal) returns a pxx vector with
%   the amplitudes and a corresponding f vector.
%
% [pxx,f] = JKWELCH3(___,'window',<arg>) applies the requested
%   window function to the windows. Default is the 'hann'
%   window.
%
% [pxx,f] = JKWELCH3(___,'fr',<arg>) applies the
%   requested frequency resolution, affecting the window
%   size utilised. Default is 0.1Hz.
%
% [pxx,f] = JKWELCH3(___,'noverlap',<arg>) applies
%   the requested overlap of the windows. Default is 50%.
%
% [pxx,f] = JKWELCH3(___,'fN',<arg>) applies
%   the requested normalisation frequency. Default is none.
%
% WINDOW FUNCTIONS
%   Valid window functions are 'hann', 'flattopwin',
%   'hamming',  'blackman', 'bartlett', 'rectwin',
%   'taylorwin', and 'triang'.
```

1

```matlab
%
% See also: Documentation on PWELCH.
%

p = inputParser;

addRequired(p, 'signal', @(x) isa(x,'struct'));
addParameter(p, 'window', 'hann', @(x) ischar(x) || isempty(x));
addParameter(p, 'fr', 0.1, @(x) isnumeric(x) && isscalar(x) ||
 isempty(x));
addParameter(p, 'noverlap' , 0.5, @(x) isnumeric(x) && isscalar(x)||
 isempty(x));
addParameter(p, 'fN', 'none', @(x) ischar(x) || isnumeric(x)||
 isempty(x));

if(nargin>1)
 parse(p, varargin{1}, varargin{2:end})
else
 parse(p, varargin{:});
end

signal = p.Results.signal;
if isempty(p.Results.window)
    window = 'hann';
else
    window = p.Results.window;
end
if isempty(p.Results.fr)
    fr = 0.1;
else
    fr = p.Results.fr;
end
if isempty(p.Results.noverlap)
    noverlap = 0.5;
else
    noverlap = p.Results.noverlap;
end
if  isnumeric(p.Results.fN) && isscalar(p.Results.fN)
    fN = p.Results.fN;
else
    fN = 1;
end

if ~isfield(signal, 'properties')
    return
else
    if ~isfield(signal.properties, 'wf_start_time')
         return
    end
end

properties = signal.properties;

fields = fieldnames(properties);
```

2

125

```
        offIndex = find(~cellfun(@isempty, regexp(fields, 'Offset')));
        scaIndex = find(~cellfun(@isempty, regexp(fields, 'Scale')));

        fs = 1/properties.wf_increment;
        c0 = properties.(fields{offIndex});
        c1 = properties.(fields{scaIndex});
        signal = c0 + signal.Values.*c1;


        wL = floor(size(signal,1)/(fs/fr));
        novlp = floor(noverlap*wL);
        wind = feval(window,floor(size(signal,1)/wL));

        [pxx,f]=pwelch(detrend(signal),wind,novlp,[],fs,'power'); %Signal,
         Window, noverlap, frequency, Sample rate
        f = f./fN;

        if nargout == 0
            assignin('base','pxx',pxx)
            assignin('base','f',f)
        end
    end
```

```
testData =

  struct with fields:

            name: 'SynchOp 20m'
    Measurements: [1×16 struct]
       Processed: [1×16 struct]
        Averages: [1×16 struct]
      Calculated: [1×16 struct]
             FFT: [1×16 struct]


FFTfield =

  1×16 struct array with fields:

    BS1
    BS2
    BS3
    BS4
    BSref
```

Published with MATLAB® R2020a

3

The *JKwelch3* function is primarily for convenience, as it only formats and structure the data so MATLABs inbuilt *pwelch* function can calculate the FFT with either a requested window type and size, or with preset default values. As a note, the window size is rather set through the users wanted resolution in the frequency, since the frequency resolution is a product of the number of samples and sampling frequency in the input signal.

```matlab
function [lower,upper] = JKcpf(varargin)
% JKcpf finds the edge values within the confidence level given
%
% SYNTAX
%   [lower,upper] = JKcpf(signal)
%   [lower,upper] = JKcpf(signal,...,'level',<arg>)
%
% INPUT
% dataset: Measured data and properties as structured by the FDB
 logger
% level: (Optional) Confidence level (Default is 0.95)
% detrend: (Optional) Specify whether the trend in the signal should
 be
% removed or not (Default is 'false')
%
% OUTPUT
% lower: Lower edge value within the level given
% upper: Upper edge value within the level given
%
% DESCRIPTION
%   Made for the structure of the output from the
%   FDB-Francislogger.
%
% [lower,upper] = JKcpf(signal) returns the lower and upper values of
 the
% input signal within the given level.
%
% [lower,upper] = JKcpf(___,'level',<arg>) sets the requested level of
% confidence for the edges. Default is 0.95.
%
% [lower,upper] = JKcpf(___,'detrend',<arg>) lets the user choose if
 the
% signal trend should be removed or not, since a signal with a slope
 will
% show a larger span between the edges than a signal without. Default
 is
% 'false'.
%
% See also: Documentation on HISTCOUNTS.

p = inputParser;

addRequired(p, 'signal', @(x) isa(x,'struct'));
addParameter(p, 'level', 0.97, @(x) isnumeric(x) && isscalar(x) ||
 isempty(x));
addParameter(p, 'detrend', false, @(x) islogical(x));

if(nargin>1)
 parse(p, varargin{1}, varargin{2:end})
else
 parse(p, varargin{:});
end
```

```matlab
signal = p.Results.signal;
if isempty(p.Results.level)
    level = 0.97;
else
    level = p.Results.level;
end

if isempty(p.Results.detrend)
    toDetrend = false;
else
    toDetrend = p.Results.detrend;
end

if toDetrend
    dataset = detrend(signal.Values);
else
    dataset = signal.Values;
end

[N,e] = histcounts(dataset,1000);
        Me = mean(dataset);
        NumberOfPoints = sum(N);

            temp=0;
        for i = 1:length(N)
            temp = temp+N(i);
            value = temp/NumberOfPoints;
            if value >= (1-level)/2
                lower = e(i);
                break;
            end
        end
            temp=0;
        for j = 1:length(N)
            temp = temp+N(j);
            value = temp/NumberOfPoints;
            if value >= level+(1-level)/2
                upper = e(j);
                break;
            end
        end
end


testData =

  struct with fields:

            name: 'SynchOp 20m'
    Measurements: [1×16 struct]
       Processed: [1×16 struct]
        Averages: [1×16 struct]
      Calculated: [1×16 struct]
```

```
exampleSensor =

  struct with fields:

       value: -0.6565
   startTime: 07-Jun-2023 17:09:59
         std: 0.1402
           N: 451000
         e_r: 6.0948e-07
         f_r: -9.2833e-07
   lowerEdge: -0.1788
   upperEdge: 0.1954
         p2p: 0.3742
```

Published with MATLAB® R2020a

130

The *JKcpf* function is used to calculate the upper and lower edges of an input signal, discarding the samples outside of the specified level, which defaults to 97% of the samples.